AGU PUBLICATIONS

JGR

Journal of Geophysical Research: Solid Earth

RESEARCH ARTICLE

10.1002/2014JB011131

Key Points:
- Modeling seafloor compliance to constrain melt distributions in oceanic crust
- The lower crust at some segments of EPR 9°–10°N may contain large amount of melt
- Evidences indicate a decrease of melt fraction following the 2005–2006 eruption

Supporting Information:
- Readme
- Figure S1
- Figure S2

Correspondence to:
Y. Zha,
yangz@ldeo.columbia.edu

Citation:
Zha, Y., S. C. Webb, S. L. Nooner, and W. C. Crawford (2014), Spatial distribution and temporal evolution of crustal melt distribution beneath the East Pacific Rise at 9°–10°N inferred from 3-D seafloor compliance modeling, *J. Geophys. Res. Solid Earth*, *119*, doi:10.1002/2014JB011131.

Received 17 MAR 2014
Accepted 29 APR 2014
Accepted article online 5 MAY 2014

Spatial distribution and temporal evolution of crustal melt distribution beneath the East Pacific Rise at 9°–10°N inferred from 3-D seafloor compliance modeling

Yang Zha[1], Spahr C. Webb[1], Scott. L. Nooner[2], and Wayne C. Crawford[3]

[1]Lamont Doherty Earth Observatory, Columbia University, Palisades, New York, USA, [2]Department of Geography and Geology, University of North Carolina at Wilmington, Wilmington, North Carolina, USA, [3]Équipe de géosciences marines, Institut de Physique du Globe de Paris, Sorbonne Paris Cité, Paris VII - Denis Diderot University, UMR 7154 CNRS, Paris, France

Abstract Determining the melt distribution in oceanic crust at mid-ocean ridges is critical to understanding how magma is transported and emplaced in the crust. Seafloor compliance—deformation under ocean wave forcing—is primarily sensitive to regions of low shear velocity in the crust, making it a useful tool to probe melt distribution. Analysis of compliance data collected at East Pacific Rise between 9° and 10°N through 3-D numerical modeling reveals strong along-axis variations in the lower crustal shear velocities, as well as temporal variation of crustal shear velocity near 9°48′N between measurements spanning 8 years. Compliance measured across the rise axis at 9°48′N and 9°33′N suggest a deep crustal low-velocity zone beneath the ridge axis, with a low *Vs/Vp* ratio consistent with melt in low aspect ratio cracks or sills. Changes in compliance measured at 9°48′N between years 1999 and 2007 suggest that the melt fraction in the axial crust decreased during this interval, perhaps following the 2005–2006 seafloor eruption. This temporal variability provides direct evidence for short-term variations of the magmatic system at a fast spreading ridge.

1. Introduction

Over two thirds of new surface on the Earth is created at oceanic spreading centers. Most of this new material is produced through partial melting of mantle peridotites beneath mid-ocean ridges [*Moores and Vine*, 1971; *Sinton and Detrick*, 1992], but little is understood about how magma travels through and is emplaced in the crust. Determining the distribution of melt in the crust is therefore important to understanding the mechanisms of crustal accretion. Seismic studies at the fast spreading East Pacific Rise (EPR) imaged a narrow, thin magma lens (usually less than 1 km wide and 10–50 m tall) beneath most of the rise axis, at depths ranging from 1.1 to 1.8 km [*Carbotte et al*., 2013; *Detrick et al*., 1987; *Kent et al*., 1993a; *Tolstoy et al*., 1997]. This thin, semicontinuous axial magma lens (AML) sits atop a broader region of low seismic velocity and high attenuation [*Wilcock et al*., 1992]. The AML has been observed to vary along axis from nearly pure melt in some sections to others that may be best described a crystalline mush [*Singh et al*., 1998]. Dikes erupt periodically from the AML to form the overlying extrusive layer, partly draining the AML. Thus, the melt content and thickness of the AML can vary temporally as melt is removed from the lens, added from below, and is cooled from above.

While active source seismic studies provide extensive details about the structure of upper crust [*Harding et al*., 1993; *Toomey et al*., 1994; *Vera et al*., 1990], seismic waves encounter significant attenuation and diffraction beneath the AML, hindering accurate interpretations of deeper structure. Seismic tomography studies of the EPR show a broader region of lowered seismic velocities (LVZ, for low-velocity zone) beneath the AML [*Vera et al*., 1990], probably representing a large partially crystalline "mush zone," believed to contain large amounts of melt [*Dunn et al*., 2000]. However, the amount of melt in the middle to lower crust and near the Moho transition zone is still largely under debate. A tomographic study by *Dunn et al*. [2000] suggests that compressional velocities increase rapidly with depth beneath the AML, indicating a decreasing melt fraction with depth in the lower crust. Other seismic reflection and seafloor compliance studies suggest the presence of a second melt lens at or near the base of the crust [*Crawford et al*., 1999; *Garmany*, 1989]. Moreover, the influence of melt fraction on seismic velocities depends heavily on the melt geometry [*Hammond and Humphreys*, 2000; *Schmeling*, 1985], making it difficult to calculate the melt fraction from the measurement of

one type of seismic velocity, for example, compressional velocities. Finally, the amount of melt in the lower crust probably varies along axis and between oceanic spreading centers, making it difficult to estimate a "typical" melt fraction.

There are generally two end-member classes of models for the accretion of oceanic crust. Based on the seismic imaging of the AML and the underlying crystalline mush zone [*Detrick et al*., 1987; *Kent et al*., 1993a; *Mutter et al*., 1988], the "gabbros glacier" model suggests that the entire oceanic crust section was formed by the crystallization and subsidence of melt at the shallow AML [*Morgan and Chen*, 1993; *Quick and Denlinger*, 1993]. The contrasting "multisills" model based on compositional variations observed in crustal gabbros in the Oman ophiolite suggests that a substantial portion of the lower layered gabbros may have formed through crystallization of melt in situ in numerous sills within the lower crust [*Boudier et al*., 1997; *Kelemen et al*., 1997; *Korenaga and Kelemen*, 1998]. The multisill model suggests the existence of molten sills in the lower crust beneath present fast spreading ridges. Therefore, the amount of melt and existence of melt sills in the lower crust have important implications for the accretion of lower crust at fast spreading ridges.

The recent discovery using seismic reflection methods of crustal melt lenses (sills) within the middle to lower crust a few kilometers off axis [*Canales et al*., 2009, 2012; *Han et al*., 2014; *Nedimovic et al*., 2005] suggests that the pooling of melt beneath permeability barriers within the crust [*Hebert and Montesi*, 2011] may be commonplace. It is unclear how these sills evolve with time. They could freeze in place, they could be resupplied by melt percolating from below, or they could drain into the AML as the permeability barriers evolve over time.

Eruptions at fast spreading ridge axes are episodic with intervals of eruptive activity interrupted by longer periods of inactivity [*Bowles et al*., 2006; *Perfit and Chadwick*, 1998; *Sinton et al*., 2002]. Any seismic study of a rise axis is a snapshot in time representing a particular stage between eruption and recharge and between tectonic and magmatic extension. *Barth and Mutter* [1996] suggest that the 9°–10°N segment of the EPR is currently generally more magmatically inflated than the 12°N segment of the EPR, based on differences in the seismic structure of these segments. Within the 9°–10°N segment, the rise axis near 9°50′N is inferred to be the region of maximum magma budget based on the seafloor morphology and subsurface structure [*Fornari et al*., 1998; *Macdonald et al*., 1988; *Toomey et al*., 2007]. Two eruptions have been observed near 9°50′N during the last 20 years: the first in 1991–1992 [*Haymon et al*., 1993] and the second in 2005–2006 [*Haymon et al*., 1993; *Soule et al*., 2007; *Tolstoy et al*., 2006]. In contrast, the lavas at the seafloor near 9°30′N appear much older by several criteria [*Bowles et al*., 2006] and were estimated to be 500–1000 years old [*Haymon et al*., 1993].

Both the redistribution of magma within the crust associated with the eruptions and changes in the thermal structure must affect the seismic structure of the oceanic crust, but the time scale of observable changes is unknown. Observations from undersea volcanoes show evolution in the size and melt content of the underlying magma chambers over scales from years to decades [*Chadwick et al*., 2006; *Nooner and Chadwick*, 2009]. The relatively short repeat times (10–15 years) for recent eruptions near 9°50′ N on the EPR [*Soule et al*., 2007] and at Axial volcano at Juan de Fuca Ridge [*Chadwick et al*., 2006, 2012] suggest that the mush zone beneath the EPR might be evolving on similarly short time scales.

Seafloor compliance is defined as the deformation of the seafloor under ocean gravity wave loading. Normalized compliance is the transfer function in frequency ω between vertical displacement $u_z(\omega)$ and differential pressure $P(\omega)$ at the seafloor, multiplied by the wave number $k(\omega)$ of the forcing waves [*Crawford and Webb*, 2002; *Crawford et al*., 1991, 1999]:

$$\eta(\omega) = k(\omega)\frac{u_z(\omega)}{P(\omega)} \tag{1}$$

The normalized compliance of a uniform half-space is constant. Compliance is mostly sensitive to the average shear modulus structure near the sensor within a radius proportional to the forcing wavelength. Compliance measurements are particularly sensitive to regions of low shear modulus [*Crawford et al*., 1991, 1998], making this a useful tool for estimating melt distribution in the crust. An advantage of compliance measurements is that the seafloor deformation is quasi-static, and so the measurements are less affected by seismic wave diffraction and attenuation in melt-rich regions than are the relatively high frequency seismic body waves. Previous compliance studies have suggested a near Moho-level melt lens at EPR 9°48′N [*Crawford et al*., 1999],

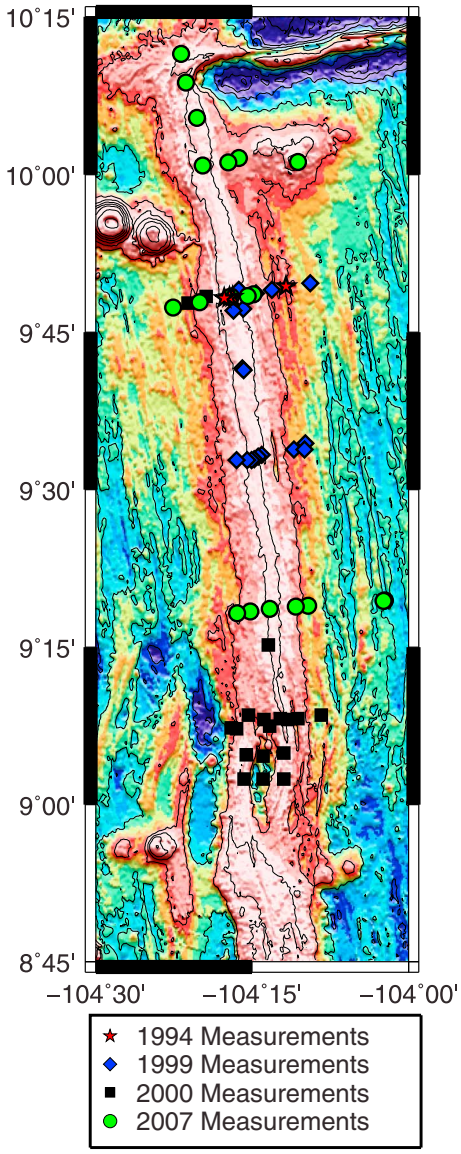

Figure 1. Bathymetric map of the East Pacific Rise 9°–10°N between the Clipperton Transform and the overlapping spreading center (OSC). Locations of 61 seafloor compliance measurement sites from four expeditions are marked in different symbols (red stars: 1994; blue diamond: 1999; black square: 2000; and green circle: 2007).

which implies that some portion of the lower crust is formed in situ. However, the seafloor compliance in these previous studies were calculated using a 2-D approximation based on 1-D numerical modeling, which underestimates the effects of rapid lateral variation of physical properties across the ridge axis, and this result needs to be tested using more accurate modeling.

In this paper we analyze compliance data collected from 1994 to 2007 at sites on the EPR 9°–10°N, using a newly developed three-dimensional seafloor compliance modeling technique. By forward modeling the effect of low shear velocity zones on compliance, we seek to provide new constraints on both the across-axis and along-axis distribution of melt in the lower crust. Our results suggest strong variation of lower crustal shear velocities along the ridge axis, with zones of very low shear velocity beneath certain segments. We also analyze repeated compliance measurements at 9°48′N to estimate the temporal change of crustal melt distribution during a period of active magmatism, especially following the 2005–2006 eruption. We discuss the implications of our results for the mechanism of crustal accretion and melt transport.

2. Data Collection

The seafloor compliance data analyzed in this paper were collected at 61 sites during expeditions in 1994, 1999, 2000, and 2007. The spatial coverage of the measurements extends from 9°03′ to 10°20′ along the ridge axis and up to 15 km off axis (Figure 1). In this paper we model crustal velocity structure using compliance data collected along four ridge-perpendicular lines: at 9°48′N, 9°33′N, 9°18′N, and 9°08′N. Long-period pressure fluctuations from ocean infragravity waves and the induced seafloor deformation are recorded by a differential pressure gauge and broadband seismometer, respectively. Compliance is then estimated by calculating the frequency-domain transfer function between the displacement and pressure signals. For the ocean depths of the EPR measurement sites (2.2 to 2.7 km), the useful compliance frequency band is approximately 0.003–0.025 Hz, corresponding to ocean infragravity wavelengths from 2 to 40 km. According to previous compliance modeling studies [*Crawford et al*., 1998, 2005; *Hulme et al*., 2005], compliance within this frequency range is sensitive to elastic properties at depths from 0 to 10 km below the seafloor. Figure 2 shows the sensitivity of compliance to shear and compressional velocities with depth (dC/d*Vs* and dC/d*Vp*, respectively). The dependence of compliance on shear velocity versus depth varies with frequency. In general, compliances at 10–18 mHz are sensitive to velocities in the upper and middle crust (0–3 km deep), and compliances $<$10 mHz are more sensitive to the lower crust and uppermost mantle (3–10 km deep). The dependence of compliance on compressional velocity variation is concentrated in the upper crust (Figure 2b); thus, variations in upper crust velocities have similar effects on compliance at all frequencies. Therefore, compliance is a good tool to study the shear velocity structure of the oceanic crust and uppermost mantle.

During analysis of the 2007 data, we discovered that the transfer function used for the differential pressure gauges in the earlier compliance measurements (1994–2000) was incorrect. The origin of the problem

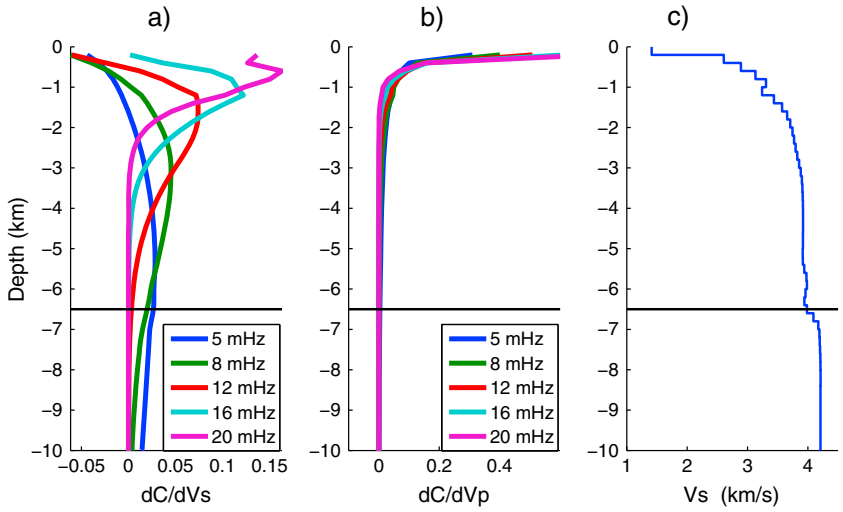

Figure 2. Sensitivity of seafloor compliance with respect to (a) *Vs* and (b) *Vp* at various frequencies. (c) The 1-D shear velocity model for calculating the sensitivity. This model is an off-axis profile from the starting 2-D model and is representative of cold oceanic crust at East Pacific Rise. Sensitivity functions are calculated using a 1-D propagator matrix method [*Crawford et al*., 1991] and normalized for each frequency. Horizontal black lines in each plot mark the Moho depth.

appears to have been an error in the in situ calibrator used for the pressure measurements in the earlier measurements. Unfortunately, the compliance meters used during these earlier measurements were dismantled, so we are unable to confirm the source of the problem. However, we were able to use records of Rayleigh waves recorded at the seabed during these measurements to determine the transfer function between the pressure sensor and seismometer and so correct the older compliance data. The maximum errors for the corrected data are less than 10%. The correction in the calibration reduces the amplitude, but not the shape of the anomalies previously discussed by *Crawford and Webb* [2002] and *Crawford et al*. [1999], implying the same subsurface features but with slightly different amplitude. We will show that 3-D effects have a stronger effect on the inferred shear velocities than the corrected calibration. The earliest compliance data described by *Crawford et al*. [1991] and *Crawford et al*. [1998] used a laboratory calibration of the pressure gauges, and those data appear to be correct.

The compliance data shown in this paper are also corrected for the effect of the gravitational attraction of the changing mass in the waves overhead of the sensor using equation (6) of *Crawford et al*. [1998] (but removing an errant factor of 2π in the exponential in the equation).

$$a_W = 2\pi G \rho_W e^{-kH} h_W \tag{2}$$

where a_W is the gravitational attraction of water, $G = 6.6732 \times 10^{-11}$ Nm^2 kg^{-3} is the gravitational constant, $\rho_W = 1040$ kg/m^3 is the density of seawater, H is the water depth, and h_W is the sea surface displacement. The apparent acceleration observed by the seismometer is the sum of the deformation under wave loading and the gravitational attraction of the waves, which is of opposite sign. After removing the gravitational attraction from the data, the actual compliance is slightly higher than apparent compliance below 5 mHz. The change in the Earth's gravitational attraction due to the displacement of the seafloor to and from the center of the Earth under wave loading also produces an apparent change in seafloor compliance, but this second gravitational term is negligible above 1 mHz.

3. Method

3.1. Numerical Modeling

Previous studies [*Crawford and Webb*, 2002; *Crawford et al*., 1991, 1999] have calculated theoretical compliance functions using 1-D propagator matrix and 2-D finite difference methods. In block inversions for shear velocity structures the compliance from a 2-D model was calculated by spatial filtering the 1-D modeling results [*Crawford et al*., 1998]. This approximation significantly underestimates the effects of lateral variation and thus biases the calculated compliance toward that of a 1-D layered structure [*Iassonov and*

Crawford, 2008]. This leads to inferring a smaller and weaker low velocity anomaly beneath the ridge axis. These models also do not account for the orientation of the forcing waves with respect to the ridge. Because crustal low-velocity zones are more continuous along the ridge axis direction, along-axis propagating ocean waves will sense a different dimension of these velocity anomalies.

In this paper we use a newly developed 3-D elastic seafloor compliance modeling technique based on finite element code *Pylith* [*Aagaard et al*., 2008; *Williams*, 2006; *Williams et al*., 2005] to more accurately calculate the compliance signal expected for a given subsurface velocity model. The velocity structure beneath the EPR 9°–10°N is relatively continuous along axis over scales of tens of kilometers, both in the uppermost mantle and beneath the AML [*Dunn et al*., 2000]. Therefore, in order to reduce the number of model parameters required, we use 2-D velocity models that are invariant and continuous along the ridge axis throughout this paper and vary the 2-D model for each cross-axis lines. We simulate ocean infragravity waves by applying sinusoidal pressure fluctuations of varying wavelengths on the top boundary of the model (the seafloor). The direction of wave propagation can be specified arbitrarily, from ridge parallel to ridge perpendicular. We show in section 4 that ocean waves propagating in a ridge-parallel direction are more sensitive to crustal low-velocity zones than waves in a ridge-perpendicular direction, leading to higher compliances. Throughout this paper, we use the conservative assumption that ocean waves propagate parallel to the ridge, if not explicitly stated otherwise. This assumption will bias the model toward slightly higher velocities (or smaller anomalies).

3.2. Model Formation

Compliance depends most strongly on shear velocities but also depends on compressional velocities and density [*Crawford et al*., 1991]. We construct a starting model based on a reference 2-D compressional velocity model from seismic refraction studies at the EPR 9°30′N by *Dunn et al*. [2000]. This model contains a midcrustal LVZ beneath the ridge axis. The velocity in the LVZ is lowest at approximately 1.5 km below seafloor and increases with depth. The LVZ is slightly asymmetric, with the lowest velocity located 0.5–1 km west of the ridge. The width of the LVZ is about 8 km. We use the symmetric component of this 2-D profile for the starting *Vp* model. We also adjust the crustal thickness from 7 km to 6 km to match recent seismic constraints [*Canales et al*., 2003]. A 1 km wide, 30 m thick axial magma lens (AML) is included in the starting model.

To convert the starting model of compressional velocity to shear velocity, we use four different *Vs-Vp* relationships depending on the expected petrology and morphology at a location. Near the spreading ridge many factors contribute to the *Vs-Vp* relationship, including high temperature, the existence of partial melt, and porosity and fracturing in the shallow crust. Thus, it is unrealistic to use a uniform relationship for the entire model. We instead divide the model into subregions and apply different *Vs-Vp* relationship to each subregion: (1) For the off-axis crust and mantle, as well as on-axis upper crust, we use a constant *Vs*/*Vp* ratio of 0.54, following *Vera et al*. [1990]. (2) The uppermost 100–200 m of the seismic layer 2A has been shown to have very low *Vs*/*Vp* ratio ($<=0.43$), due to extensive fractures and high porosity [*Vera et al*., 1990]. We use $Vs/Vp = 0.43$ for the top 100 m of our models. (3) We define the axial accretion zone as 1.2 to 9 km below the seafloor and within 4 km of the ridge axis. In this region the *Vs-Vp* relationship is largely controlled by temperature and the presence and geometry of partial melt. Rock mechanics experiments show that incremental changes in *Vs* and *Vp* can be related as $\mathrm{d}\ln Vs/\mathrm{d}\ln Vp = \alpha$ [*Takei*, 2002], where α range from 1.0 to 2.3 depending on the melt geometry. In the starting model we use $\alpha = 1.5$, which corresponds to the upper bound of textually equilibrated partially molten rocks [*Takei*, 2002]. This model gives a lowest *Vs* of ~2.0 km/s near the AML. In section 4 we use the compliance data from 9°33′N to determine the best fitting values of α. Then we use this same value of α throughout the axial accretion zone to fit the complete compliance data set. This relationship requires a starting "melt-free" value of *Vp* and *Vs*. We use $Vp = 7.2$ km/s, $Vs = 3.9$ km/s for the crust, and $Vp = 8.2$ km/s, $Vs = 4.4$ km/s for the mantle. The starting shear velocity model is shown in Figure 3.

The *Vs-Vp* relationship of partially molten rock also depends on the frequency of the wave, due to anelastic effects [*Kampfmann and Berckhemer*, 1985; *McCarthy and Takei*, 2011]. We expect *Vs* at compliance frequencies (0.005–0.02 Hz) to be lower than *Vs* at seismic frequencies (~5 Hz). However, the amplitude of this difference is highly uncertain, and simultaneously interpreting compliance due to elastic and anelastic effects in a viscoelastic media is beyond the scope of this paper. We therefore incorporate the effects of anelastic dispersion into the α parameter of the shear velocity model and do not independently consider the frequency dependence of *Vs-Vp* relationship within the compliance frequency band.

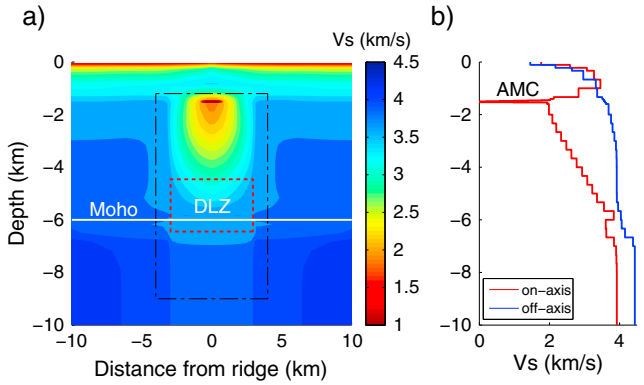

Figure 3. Starting velocity model for compliance modeling. (a) Two-dimensional starting *Vs* profile calculated from *Vp* reference model by *Dunn et al*. [2000] using a block-wise *Vs-Vp* relationship (see text for details). White horizontal line indicates depth of Moho; black dashed box indicates axial accretion zone (8 km wide and from 1.2 to 9 km depth), where *Vs-Vp* relationship for partially molten rock is used to calculate *Vs* (dln*Vs*/dln*Vp* = 1.5) [*Takei*, 2002]. Small red dashed box indicates possible deep lower crustal low-velocity zone (DLZ). (b) One-dimensional on-axis and off-axis shear velocity profiles in the starting model.

We use a 1-D density model calculated from the off-axis *Vp* profile using the relationship $\rho = 1.85 + 0.165Vp$ for basalts [*Christensen and Shaw*, 1970]. We extend this relationship through to the mantle, because compliance is very weakly dependent on density. In fact, compliance depends only on the Lamé parameter λ and the shear modulus μ of the model, but when we constrain seismic velocities *Vp* and *Vs*, compliance becomes weakly sensitive to density through the dependence of seismic velocity on density.

3.3. Model Fitting

We first use the compliance data at 9°33′N and a *Vp* model modified from *Dunn et al*. [2000] to calibrate the *Vs-Vp* relationship in the axial accretion zone. Then we search over a set of model parameters to determine preferred models for each of the ridge-perpendicular lines (9°48′N, 9°33′N, 9°18′N, and 9°08′N). We modify the thickness and shear velocities in layer 2A as well as the width and shear velocity in the midcrustal LVZ. The width of the LVZ is modified by widening or narrowing the LVZ to best fit the data while keeping its relative shape. In addition to varying the velocity and geometry of the LVZ and AML, we introduce a deep crustal low-velocity zone (DLZ) (Figure 3) where varying the other parameters cannot satisfactorily fit the compliance data. We vary its depth, size, and velocity to best fit the compliance data. The shear velocity is assumed to be constant within the DLZ. We evaluate a large suite of models by calculating the chi-square misfit χ^2 between the model prediction and the data:

$$\chi^2 = \frac{\sum_i \sum_j \left[\left(D_{ij} - S_{ij}(m) \right) / \sigma_{ij} \right]^2}{N} \tag{3}$$

where *i* runs over the measurement frequencies, *j* over the sites, D_{ij} is the measured compliance and $S_{ij}(m)$ is the calculated compliance for model *m*, σ_{ij} is the standard deviation of the measurement, and *N* is the total number of data. The preferred velocity model for each ridge-perpendicular line is the one that minimizes χ^2.

4. Results

In previous 1-D modeling studies, the higher-frequency compliance peak observed near 14 mHz at sites on the ridge axis was considered to be the effect of a molten axial magma lens (AML) with near-zero shear velocity [*Crawford et al*., 1991]. However, the 1-D approximation significantly underestimates the effect of lateral variations in structure. At 9°–10°N on the EPR the AML imaged by seismic reflection typically ranges from 500 to 1000 m wide, with exceptions near the 9°03′ overlapping spreading centers (OSC) [*Kent et al*., 1993b]. In order to quantify the effects of a realistic melt lens, we calculated compliance variation due to AMLs of different widths, thicknesses, and shear velocities. Compliance are calculated from the starting *Vs* model constructed using $\alpha = 2.0$, with an AML at 1.5 km depth. Figure 4 shows that compliance is quite insensitive to shear velocities in a 100 m tall, 1 km wide melt lens. Furthermore, only when the width of the lens exceeds 2 km does its low shear velocity appreciably affect the compliance signals. Therefore, the narrow AML (< = 1 km) observed at 9°50′N on the EPR is likely too narrow to be resolved by compliance observations. This is consistent with the previous 2-D modeling study of *Iassonov and Crawford* [2008]. Based on this sensitivity study, we conclude that the along-ridge variation of compliance observed at the EPR is mostly due to variations in the shear velocities within the LVZ beneath the AML, rather than with the velocity and thickness of the AML.

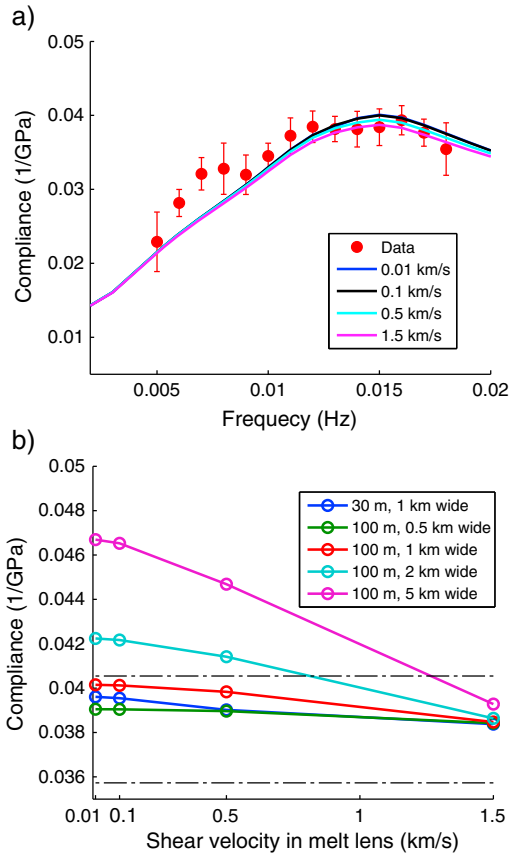

Figure 4. Effects of AML on compliances. (a) On-axis compliance from the shear velocity models with a 30 m thick, 1 km wide AML of different shear velocities. AML is located 1500 m below seafloor at ridge axis ($\alpha = 2.0$ for converting *Vp* to *Vs*, following previous discussions). On-axis compliance data from 9°48 are shown as comparison. (b) Sensitivity of on-axis compliance at 14 mHz to shear velocity within the AML, calculated for different AML geometries. Two dashed horizontal lines mark the range of measured compliance value at 9°48′N (± standard deviation).

In modeling a molten magma lens, instead of setting $Vs = 0$, we use a very small velocity $Vs = 0.01$ km/s for computational stability. *Hulme et al.* [2005] have demonstrated analytically that the compliance of a $Vs = 0.01$ km/s body is indistinguishable from that of a $Vs = 0$ km/s body. Any shear velocity of the subsurface lower than the forcing ocean wave phase velocity (0.05–0.2 km/s for the frequency range of these compliance measurements) produces a similar compliance signal.

4.1. Effects of Ocean Wave Direction

Previous 2-D modeling studies calculated compliance induced by ocean waves propagating perpendicular to the ridge. Observations show the typical mid-ocean infragravity wave field includes waves propagating from a wide range of directions [*Webb et al.*, 1991]. Because of the quasi-2-D characteristics of fast spreading mid-ocean ridges, ocean waves propagating in different direction will have different contributions to compliance. Quantifying the variation of compliance with wave azimuth can yield information on the uncertainty of inferred velocity models due to a varying wave field.

To quantify the effects of ocean wave direction, we calculated compliance induced by ocean waves with orientations ranging from ridge parallel to ridge perpendicular (Figure 5). At lower frequencies ($f < 10$ mHz), where compliance observations are more sensitive to lower crust and mantle velocities, compliance is highest when the ocean waves propagate parallel to the ridge and decreases with increasing angle between the wave direction and the ridge axis (Figure 5). This is because the LVZ in our model is invariant and continuous along the ridge axis dimension. Ocean waves in this direction sense a "wider" LVZ, producing higher compliance. Compliance over a melt body ($Vs = 0.01$ km/s) is also more sensitive to ocean wave direction than is compliance of a mush zone ($Vs = 1$ km/s). The difference between compliance signals induced by ridge-parallel and ridge-perpendicular ocean waves at 5 mHz is approximately 10% for a mush zone and 15% for a melt body. At higher frequencies ($f > 15$ mHz), compliance is about 5% lower for ridge-parallel waves than for ridge-perpendicular waves (Figure 5). This is because the low-velocity pillow basalt layer (layer 2A) is thinnest at the ridge axis; thus, ridge-parallel waves are sensing a thinner 2A layer than do ridge-perpendicular waves. We did not measure the directional spectrum of the infragravity waves during the compliance observations due to lack of simultaneous measurements, so we will use the conservative assumption that the waves propagate along axis, which may bias the middle and lower crust in the resulting models toward slightly higher shear velocities.

4.2. Calibrating the *Vs-Vp* Relationship

We first determine the best fitting *Vs-Vp* relationship for the axial accretion zone using compliance measured at 9°33′N. A series of *Vs* models are generated using the starting *Vp* model and different α ($\alpha = \mathrm{d}\ln Vs / \mathrm{d}\ln Vp$); then the optimal value of α is chosen to minimize the χ^2 misfit between the predicted compliance and the data, as a function of both frequency and distance from the ridge axis. Figure 6 compares on-axis compliance data at 9°33′N with synthetic compliance calculated from five different *Vs* models corresponding to $\alpha = 1,\ 1.5,\ 1.8,\ 2.0$ and 2.2 (Figure 6b). Since α is the ratio of the fractional change between *Vp* and *Vs*,

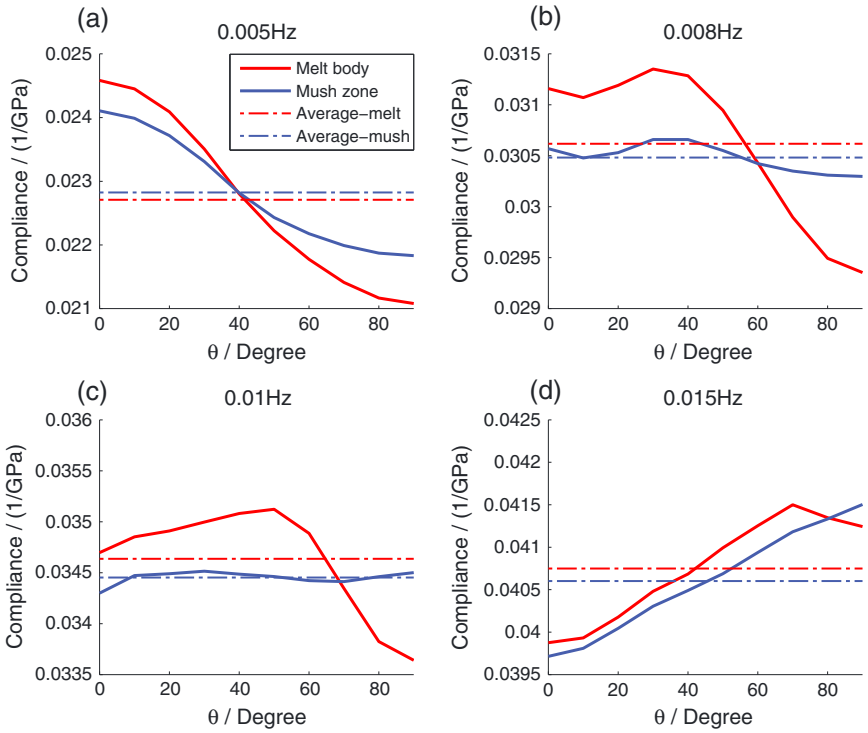

Figure 5. On-axis compliance (solid curves) calculated from 3-D models with melt lens (red) or mush zone (blue) as a function of angle between ocean wave direction and the ridge axis. 0° corresponds to ridge-parallel wave, and 90° corresponds to ridge-perpendicular wave. Properties of low-velocity bodies: melt lens: 3 km wide, 700 m tall, *Vs* = 0.01 km/s and mush zone (blue): 3 km wide, 2 km tall, *Vs* = 1 km/s. Melt and mush zones are both continuous along axis. Top of both bodies are located 4 km below seafloor. (a) 0.005 Hz, (b) 0.008 Hz, (c) 0.01 Hz, and (d) 0.015 Hz. Thin dashed flat lines are direction-averaged compliance for each frequency. Model dimension: 100 km (wide) × 100 km (tall) × 30 km (along axis).

changing α will have a larger effect on *Vs* where the *Vp* anomaly is larger, i.e., within the LVZ. Changing *Vs* in the LVZ (1.5–4 km below seafloor) mostly affects compliances at frequencies above 10 mHz (Figure 2). Therefore, we calculate the misfit of each model both (1) over all frequencies and (2) over the higher-frequency band (11–18 mHz) (Table 1), and we choose the α that minimizes both. Assuming a constant *Vs*/*Vp* ratio ($\alpha = 1$) or the commonly assumed $\alpha = 1.5$ significantly underestimates on-axis compliances, especially between 11 and 18 mHz ($\chi^2_{\text{on axis}} = 74.6$ and 23.9, respectively). The compliance in this frequency range requires a lower shear velocity within the LVZ (1.5–4 km below seafloor) and therefore a higher value of α. A model with $\alpha = 2.0$ has the lowest total misfit over all frequencies ($\chi^2 = 3.2$). In the high-frequency band (11–18 mHz), models with $\alpha = 1.8$ and $\alpha = 2.0$ both have low total misfit ($\chi^2 = 2.2$ for $\alpha = 1.8$ and $\chi^2 = 2.6$ for $\alpha = 2.0$), but the on-axis misfit for the $\alpha = 1.8$ model ($\chi^2 = 6.6$) is significantly higher than that of the $\alpha = 2.0$ model ($\chi^2 = 3.2$). Therefore, we use $\alpha = 2.0$ to relate *Vp* and *Vs* throughout this paper. This model indicates a lowest LVZ shear velocity of approximately 1.5 km/s beneath the AML. Four different *Vs*-*Vp* relationships used in the modeling are illustrated in Figure 6c. For the same reduction in *Vp*, *Vs* reduction will be larger for partially molten crust and mantle (red and green curves, respectively) than for normal, melt-free crust and mantle (blue straight line). We note here again that this relationship was obtained using frequencies 2–3 orders of magnitude lower than active source seismic frequencies. Due to anelastic dispersion effects, the shear velocities at active source seismic frequencies near 5 Hz should be slightly higher than those indicated by compliance measurements.

We note that although the starting *Vp* model and a proper *Vs*-*Vp* relationship fit high-frequency compliance data reasonably well ($\chi^2 < 3$), these models all underestimate compliance below 10 mHz, which are mostly controlled by lower crustal velocities.

4.3. Deep Low Velocity Zone at 9°48′N

Compliance measurements near EPR 9°48′N show a broadband peak near 14 mHz and a lower frequency peak at 8 mHz (Figure 7). The higher-frequency peak near 14 mHz can be fit by adjusting the *Vs*-*Vp*

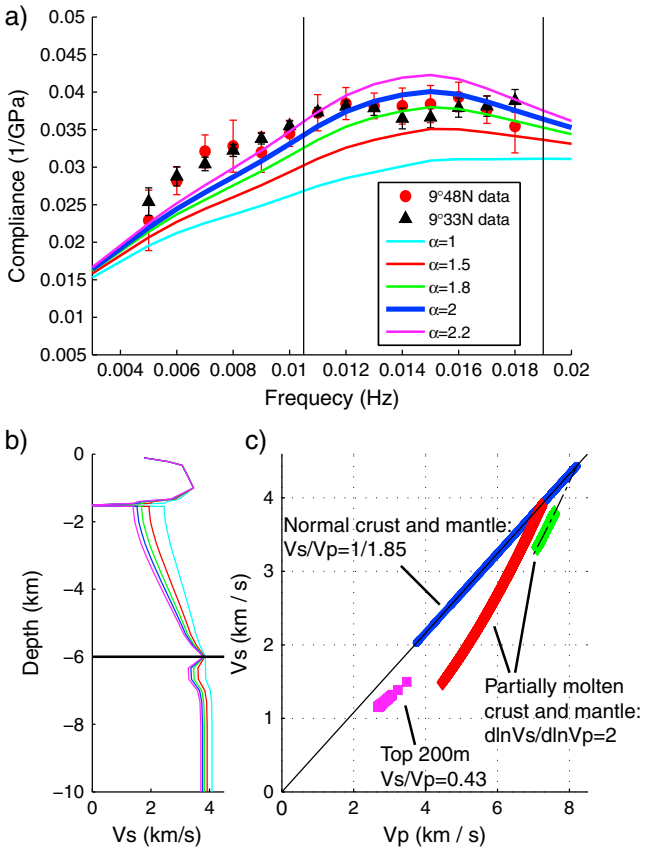

Figure 6. Using compliance to calibrate *Vs-Vp* relationships. (a) On-axis compliance data at 9°33′N (red solid circles) and compliance prediction (solid and dashed curves) of five models with different α ($\alpha = \mathrm{dln}Vs/\mathrm{dln}Vp$, see text for details). Vertical thin lines indicate frequency range (0.011–0.018 Hz) used to evaluate model misfit and to select proper value of α. Solid blue curve corresponds to $\alpha = 2$, the preferred value. (b) On-axis 1-D *Vs* profiles of using same *Vp* profile but different α. Horizontal line marks the Moho. (c) *Vs-Vp* relationship used to calculate shear velocities from compressional velocity models. Blue: constant *Vs/Vp* ratio applied to off-axis crust and mantle, following *Vera et al.* [1990]; purple: top 200 m of layer 2A, red: *Vs-Vp* relationship for partially molten rocks applied to axial middle and lower crust (<4 km from the ridge, between 1.2 km deep and the Moho), according to *Takei* [2002]. Green: same *Vs-Vp* relationship as red but for mantle partial melt zone, (<4 km from the ridge, 6–9 km deep).

relationship so that the shear velocity is lower in the shallow LVZ. The lower frequency compliance peak near 8 mHz, on the other hand, is less sensitive to the shallow LVZ. Matching the low-frequency compliances requires lower shear velocities in the deep lower crust and uppermost mantle (4–9 km below seafloor). We tested a large suite of velocity models to find the shear velocity structure that best reproduces the compliance signatures observed in the data. In order to prevent unnecessary extra structure, when searching for a "best fitting" model, we started with a model without a DLZ, then we reduced the remaining compliance misfit by adding DLZs of various geometries and constant velocities. Because the shear velocity anomaly in the lower crust requires near-solidus temperatures, we assume that the DLZ boundary roughly follows an isotherm. Throughout this paper, we use a DLZ geometry that is widest at the base and narrows toward the top. We note that the blocky shape of the DLZ in our models should not be interpreted as a precise description of the anomaly.

The best fitting model for 9°48′N has a midcrustal LVZ from 1.5 to 4 km below seafloor, with a minimum velocity of 1.5 km/s just beneath the AML. The width of the LVZ is approximately 5–7 km, consistent with the LVZ width imaged by seismic tomography at 9°50′N [*Canales et al.*, 2012] and 9°33′N [*Dunn et al.*, 2000]. In addition to the shallow LVZ, the compliance data also indicate a DLZ from 4 km to 7 km below the seafloor, extending into the top of mantle (Figure 8). Figure 7 compares the on-axis compliance measurements and predicted compliances using several models, including the starting model. The model misfits are summarized in Table 2. Compliance calculated using the starting model (model 1,

Table 1. Misfit χ^2 of Velocity Models With Different Value of α for 9°33′N Data[a]

α	χ^2_{total} (5–18 mHz)	$\chi^2_{\mathrm{on\ axis}}$ (11–18 mHz)	χ^2_{total} (11–18 mHz)	χ^2_{total} (5–10 mHz)
1.0	18.8	74.6	12.7	25.3
1.5	7.9	23.9	4.2	12.3
1.8	3.6	6.6	2.2	4.5
2.0	3.2	3.2	2.6	3.9
2.2	3.9	7.7	4.7	2.6

[a]See text for details, $\alpha = \mathrm{dln}Vs/\mathrm{dln}Vp$ [*Takei*, 2002] is used to calculate *Vs* from reference *Vp* model. All models use same *Vp* and density model. A $\alpha = 1.5$ starting model is shown in Figure 3.

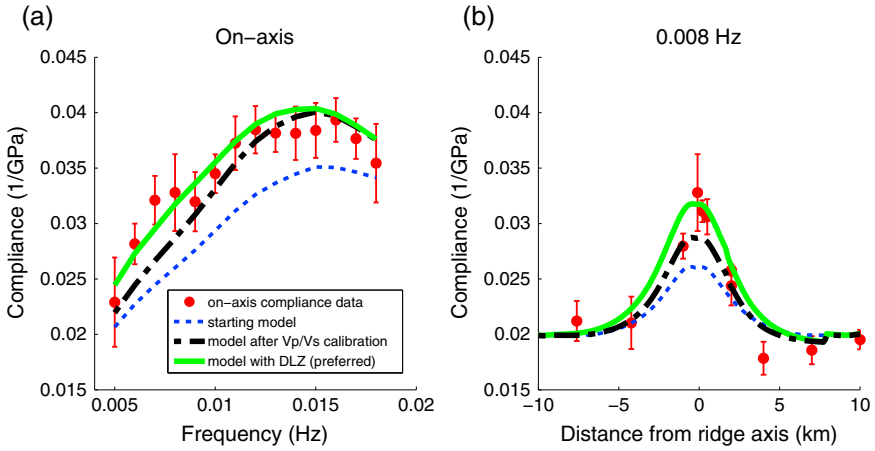

Figure 7. Compliance measurements at 9°48′N and calculated forward compliance from different models. (a) Compliance as a function of frequency at ridge axis. (b) Compliance as a function of distance from the ridge crest at 8 mHz, which is sensitive to lower crustal shear velocities (Figure 2). Red circle: measurements prior to 2007 with error bars; dashed blue curve: model 1, starting model derived from *P* wave velocity model by *Dunn et al.* [2000]; dash-dotted black curve: model 2, after calibration *Vs-Vp* relationship using $\alpha = 2.0$; solid green curve: preferred model (model 3), similar to model 2 but with a deep low-velocity zone (DLZ) in the lower crust, 4–7 km below the seafloor with an shear velocity of 1.5 km/s. Shear wave velocity profiles with depth for each model are shown in Figure 8a. See Table 1 for detailed summary of each model.

$\alpha = 1.5$) is too low to fit the data at nearly all frequencies, both on and off axis (on-axis $\chi^2 = 19.4$, overall $\chi^2 = 7.3$). After adjusting the shear velocities using a calibrated *Vs-Vp* relationship ($\alpha = 2.0$), model 2 (without a DLZ) has much lower misfit in the high-frequency range ($\chi^2 = 2.6$, $f > 10$ mHz) but predicted that compliances at lower frequencies are still too low to explain the data (on-axis $\chi^2 = 5.3$, low-frequency overall $\chi^2 = 4.0$). Figure S1 in the supporting information shows a comparison of calculated compliance between DLZs of different shear velocities. The best fitting model (model 3) adds a 3 km tall DLZ that is 4 km wide near its base and which has a *Vs* of 1.5 km/s (*Vp* = 4.5 km/s).

Previous compliance studies have suggested that a Moho-level pure melt lens, one that is deeper and perhaps larger than the AML, may exist at EPR 9°48′N and can explain the anomalous compliance peak [*Crawford et al.*, 1999]. However, we show that due to the limited resolving power of compliance to subwavelength features, even a 2 km wide, 300 m thick melt lens located just below the Moho at 6 km depth

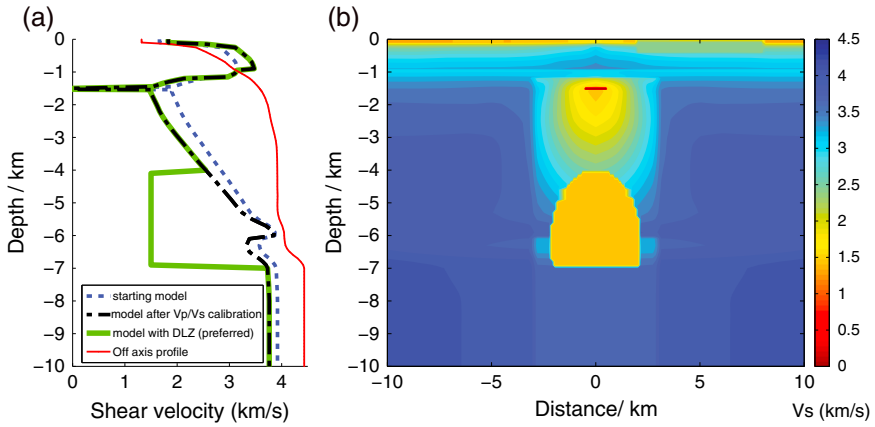

Figure 8. (a) One-dimensional shear velocity profile of models calculated in Figure 7. Dashed blue curve: (model 1) reference *Vs* model derived from *Vp* model by *Dunn et al.* [2000], using a starting value of $\alpha = 1.5$; dash-dotted black curve (model 2): *Vs* model calculated using $\alpha = 2.0$, with lower shear velocity in the midcrust than the reference model; solid green curve (model 3): our preferred model with a deep low-velocity zone (DLZ), 4–7 km below the seafloor; red curve: off-axis velocity profile for old, off-axis crust at 50 km from the ridge; crustal thickness is 6 km. (b) Preferred 2-D *Vs* model (model 3) for EPR 9°48′N suggested by compliance modeling, with DLZ beneath the ridge crest.

Table 2. Compliance Misfit χ^2 of Different Velocity Models for 9°48′N Data[a]

Model	χ^2_{total}	$\chi^2_{on\ axis}$ (0–0.5 km)	χ^2_{low} (5–10 mHz)	χ^2_{high} (11–18 mHz)
1	7.3	19.4	11.6	4.4
2	3.2	5.3	4.0	2.6
3	2.6	1.7	2.0	2.9

[a]Model 1: starting model converted using symmetric reference *Vp* model, $\alpha = 1.5$; model 2: model after calibration of *Vp*/*Vs* relation, $\alpha = 2.0$; model 3: modified from model 2 by adding a 4 km wide, 3 km tall deep low-velocity zone (DLZ) of *Vs* = 1.5 km/s at 4 km depth. χ^2_{total} is calculated from all measurements 5–18 mHz and within 10 km from ridge axis.

will have negligible effect on the on-axis compliance (Figure S1). No melt bodies of similar or larger scale have been reported by seismic reflection studies. Therefore, we conclude that the observed compliance anomaly cannot be solely explained by a single Moho-level melt lens.

Although the geometry of the DLZ is an over simplification, this model provides an estimate of the average effective shear modulus over a 2–5 km thick region at compliance frequencies (5–20 mHz). The shear velocity in the DLZ is approximately 30%–60% lower than the velocity inferred from the starting model, which increases from 3 km/s at 4 km depth to 4 km/s at 7 km depth using the relationship between *Vp* and *Vs* described above. The deep DLZ and the shallow LVZ (Figure 8) do not need to be separated by a high-velocity region. We inserted a discrete DLZ into the starting model in order to minimize the number of model parameters, but a model with smooth shear velocity transition from the LVZ to the DLZ may fit the compliance data as well. The calculation of 2-D smoothed models from the compliance data will be the subject of future studies.

In the higher-frequency range (>11 mHz), compliance measurements at various frequencies are asymmetric with respect to the ridge. Compliance measured from 3 to 7 km east of the ridge are lower than compliance measured at similar distances to the west, suggesting a higher upper crustal velocity to the east of the ridge. This asymmetry can be accounted for by increasing the shear velocity in the upper 100 m by 0.8 km/s at distances from 3 to 7 km east of the ridge. This is likely a result of thinner layer 2A.

Our estimates of shear velocity are based on the assumption that the forcing ocean wave propagates along axis and that the DLZ is continuous along the axis. As discussed in section 4.1, this assumption gives a conservative estimate of the shear velocity anomaly in the LVZ and DLZ, if they are relatively continuous along axis. The LVZ beneath this well-studied section of EPR has been shown to be relatively continuous both in the uppermost mantle and beneath the AML over tens of kilometers [*Dunn et al*., 2000], suggesting that a continuous LVZ is a reasonable simplification.

4.4. Temporal Changes of Compliance Measurements and Inferred Structures Near 9°48′N From 1994 to 2007

During 2005–2006, the EPR near 9°48′N erupted a thick layer of lava onto the seafloor along 18 km of the rise axis [*Soule et al*., 2007]. On-axis compliance measurements at 9°48′N in 2007 experiment showed a decrease in compliance at nearly all measured frequencies compared to the previous measurements (1994 and 1999), with the largest decrease between 7 and 14 mHz (Figure 9a). Compared to the large decrease of compliance from 1999 to 2007, differences between the 1994 and 1999 on-axis measurements are nearly negligible, except for a small decrease near 8 mHz. This result indicates an increase in crustal shear velocities between 1999 and 2007. An increase of shear velocity could occur in the AML, LVZ, or the DLZ. But our sensitivity study earlier this section showed that changes of shear velocity in the AML are not likely to significantly affect the compliance signal (Figure 4). Even if *Vs* in a 100 m tall, 1 km wide AML increases from 0.01 km/s to 1.5 km/s, the change of compliance is only 2% at 14 mHz, much less than the observed 20% decrease in the data. We modeled the observed decrease of on-axis compliance as simply as possible by changing the shear velocities in the LVZ and DLZ. We searched for the models that best fit the posteruption compliance data using the same procedure as described in section 2 while keeping the same upper crustal velocity model. The best fitting posteruption model includes higher velocities in both the LVZ and DLZ (Figure 9). In the LVZ, shear velocities increase by up to 0.6 km/s (the minimum shear velocity increases from 1.5 km/s to 2.1 km/s). The presence of a DLZ is still preferred, giving a slightly lower overall misfit ($\chi^2 = 2.50$) than a model without the

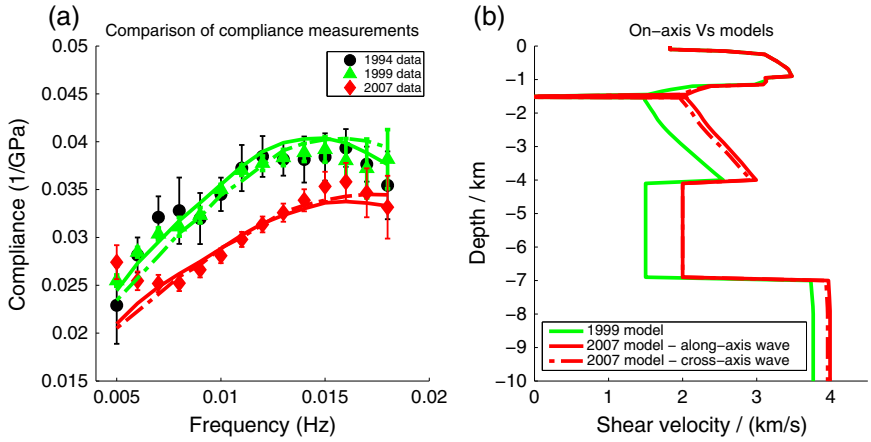

Figure 9. Comparison of preeruption and posteruption compliance measurements at EPR 9°48′N. (a) On-axis compliance measurements and uncertainties with model predictions (solid and dash lines). Green solid: preferred model for 1999 data; green dashed: same model as green solid but assuming ridge-perpendicular ocean wave; red solid: preferred model for 2007 data assuming ridge-parallel ocean wave; red dashed: preferred model for 2007 data assuming ridge perpendicular ocean wave. (b) Comparison of on-axis velocity profiles corresponding to 1999 and 2007 data. Geometry of DLZ is same as illustrated in Figure 8.

DLZ ($\chi^2 = 2.96$), but compliance in 2007 is much more sensitive to the LVZ than to the DLZ (Figure S2), so we cannot determine if there is a change in DLZ velocities after the 2005–2006 eruption.

In section 4.1 we showed that the direction of the forcing infragravity waves can also affect compliance. A small part of the observed changes in on-axis compliance from 1999 to 2007 could be caused by changes in the wave direction, but even the most extreme change in wave direction (from purely ridge parallel in 1999 to purely ridge perpendicular in 2007) would only decrease compliance by 3–5%, much less than the observed ~20% change in compliance (Figure 9a). Furthermore, we have obtained alternate best fit models for 2007 data assuming either ridge-parallel or ridge-perpendicular wave directions (Figure 9b). The difference between these two models is also much smaller than their differences with the preeruption model. Therefore, we conclude that the observed decrease in on-axis compliances can be mainly attributed to the increase of shear velocities within the axial LVZ.

4.5. Along-Axis Variation of Lower Crustal Velocity Structure

To study the along-axis variation of the melt distribution, we analyzed compliance data from three other ridge-perpendicular lines, crossing the rise axis at 9°33′N, 9°18′N, and 9°08′N. The latter line is at the northern end of an overlapping spreading center (OSC) near 9°03′N. We search for the best fitting models for these lines, following the procedure discussed previously. Because the upper crust structure is different for each line, we first determine appropriate layer 2A velocities and thicknesses by fitting only the higher-frequency compliance data then add lower-frequency data to determine best fitting velocities for the LVZ and DLZ. The DLZ is not added unless it is required to fit the data. Figure 10 shows on-axis compliance measurements compared to forward calculations (top row), the cross-axis compliance at 10 mHz (middle row), and the preferred models (bottom row). To facilitate comparison, the compliance data at 9°48′N are shown as grey circles in the top two row.

4.5.1. Compliance at 9°33′N

Compliances at 9°33′N are quite similar to those at 9°48′N both in terms of frequency dependence and cross-axis shape (Figure 10a). Compliance at 10 mHz is higher 0.5 km west of the rise axis than at the rise axis [*Crawford and Webb*, 2002]. The preferred velocity structure at 9°33′N is also similar to that at 9°48′N, with a 5 km wide LVZ and a DLZ. The lowest shear velocity in the LVZ is approximately 1.5 km/s, but the center of the LVZ is offset 0.6 km to the west of the ridge crest. This misalignment agrees with previous seismic tomographic model with the lowest *Vp* located 0.5–1 km west of the ridge [*Dunn et al.*, 2000]. In the lower crust, a DLZ is also preferred by the on-axis compliance data. The best fitting model has a 4 km wide, 3 km tall DLZ, with $Vs = 2.0$ km/s ($Vp = 5.2$ km/s). This model yields an on-axis compliance misfit of $\chi^2 = 2.80$, whereas a

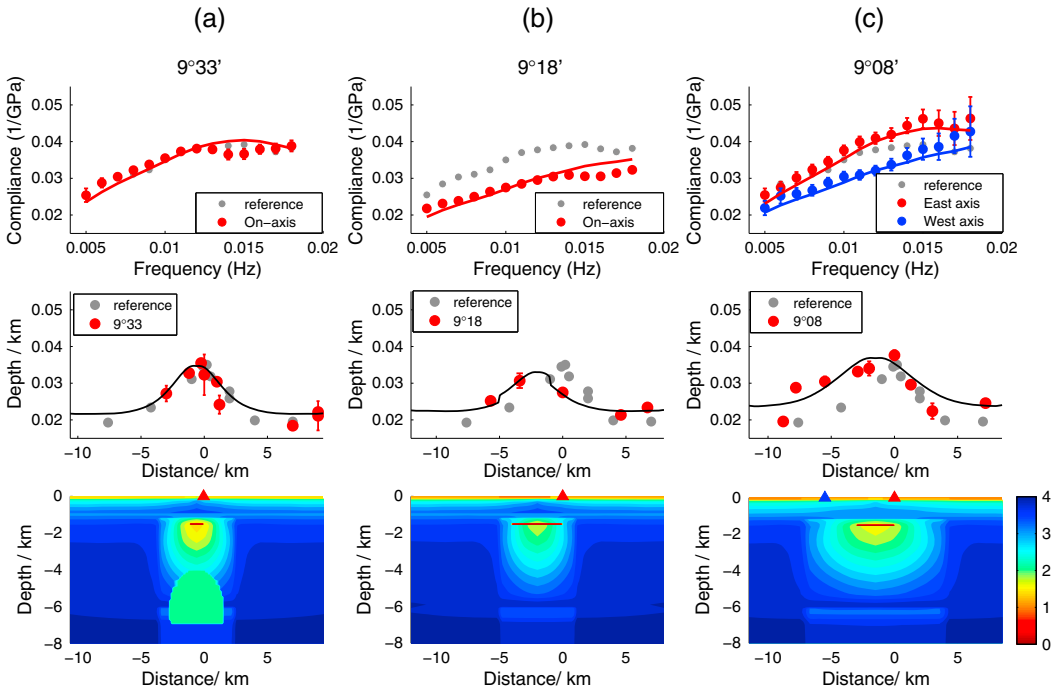

Figure 10. Compliance measurements and preferred models at different locations along the EPR 9°–10°N (see text for details). Top row: On-axis compliance (solid circles with error bars) and model predictions (solid curves); Measurement sites corresponding to red and blue solid circles are shown in red and blue triangles in the bottom row, respectively. At 9°08′N both the east and west axis measurements are shown. Compliances at 9°48′N are shown in grey circles for comparison. Middle row: compliances at 10 mHz as a function of distance from ridge axis (red solid circles: data; grey solid circles: reference compliances at 9°48′N; thin black curves: model predictions). Bottom row: preferred 2-D shear velocity models for each location. Locations of on-axis compliance site shown in the bottom row are marked as solid triangles. (a) 9°33′N; (b) 9°18′N; and (c) 9°08′N.

model without a DLZ has $\chi^2 = 7.84$. The DLZ shear velocity at 9°33′N is higher than at 9°48′N (2.0 km/s compared to 1.5 km/s). We will discuss the implication of this along-axis variation of DLZ in section 5.

4.5.2. Compliance at 9°18′N

Compliance at 9°18′N is characterized by a strong asymmetry across the rise axis, especially at high frequencies (>0.01 Hz). The on-axis compliances at 9°18′N are lower than those at 9°48′N and 9°33′N at all frequencies, and compliance is higher 3.4 km west of the rise axis than on axis (Figure 10b). The differences between these two sites (on axis and 3.4 km west) are greatest at the higher frequencies, suggesting that most of the anomalous high compliance west of the axis is caused by a slower upper crust. Previous multichannel seismic reflection studies revealed a large AML up to 4.15 km wide near 9°17′N [*Kent et al.*, 1993a] and a thicker than normal extrusive layer 2A to the west of the wide AML [*Harding et al.*, 1993]. We suggest that the higher-compliance anomaly to the west of the ridge crest is a result of both the westward shift of the AML/LVZ with respect to the ridge and a thicker 2A layer. In modeling the 9°18′N data, we use an AML 4 km wide and centered 1 km west of the axis. Due to the complex asymmetry in the data, we did not try to fit compliance functions at all the sites. We instead fit only the two measurements closest to the ridge crest in order to obtain a first-order estimate of the amplitude of the crustal shear velocity anomaly.

In our preferred model for 9°18′N (Figure 10b), the upper 100 m of layer 2A west of the axis is slower than normal, with a shear velocity of 1.0 km/s compared to 1.4 km/s on the eastern side. In the midcrust, the center of the LVZ is located 2 km to the west of the axis. Despite a very wide AML imaged, the velocity anomaly in the LVZ is smaller than that of 9°48′N and 9°33′N, with a relative amplitude of 0.8 and minimum *Vs* of 1.8 km/s. Unlike 9°33′N and 9°48′N, a DLZ in the lower crust is not required by the data. This does not exclude the possibility of a smaller DLZ or one with higher velocities. Because of the decaying resolution of compliance with depth, a small DLZ near the base of the crust with lateral dimensions less than 1 km can neither be ruled out nor required in the models.

4.5.3. Compliance at 9°08′N

The 9°08′N measurement line crosses the ridge axis at the eastern limb of the 9°03′N overlapping spreading center (OSC). The eastern limb propagates southward and is currently replacing the western limb as the main axis of spreading [*Macdonald et al*., 1988]. In this area the upper crust melt lens beneath the eastern limb was also imaged to be 3–4 km wide [*Kent et al*., 2000]. Compliance measurements exhibit a broad, asymmetric peak at 8–14 mHz: compliance at 10 mHz is highest at the eastern limb axis, rapidly decreasing to the east (Figure 10c) but slowly decreasing to the west, toward the northern tip of the western axis. West of the western axis, compliance again drops off rapidly [*Crawford and Webb*, 2002].

High compliances between the east and west limb axis suggest that both the eastern and western limb influence this LVZ even though the line is north of the overlap basin. Similar to 9°18′N, compliance data near 9°08′N are highly asymmetric and cannot be fit by a symmetric model. We vary the width, amplitude of velocity anomaly of the LVZ, and its lateral position relative to the ridge axis in order to find a model that minimizes compliance misfits for the eastern and western axis only.

The best fit LVZ at 9°08′N is about 13 km wide, more than twice as wide as LVZs at all other locations. The lowest velocity in the LVZ is approximately 1.65 km/s and lies between the eastern limb and western limb of the OSC, closer to the eastern limb axis (offset ~1.5 km) (Figure 10c). This is consistent with seismic tomography studies that place the strongest velocity anomaly west of the eastern limb axis [*Bazin et al*., 2003; *Tong et al*., 2003]. Although an anomalously wide LVZ and AML are suggested beneath the 9°08′N line, a DLZ is not required by compliance data. This model yield an on-axis misfit of $\chi^2 = 0.92$, but the overall misfit is still high ($\chi^2 = 5.71$). The greater complexity of crustal structure at 9°18′N and 9°08′N suggests that a full 2-D compliance inversion technique without prior assumptions of discrete blocks is needed to resolve the finer-scale structure. The development of such inversion scheme will be investigated in future studies.

5. Discussion

5.1. The DLZ: Implication for Crustal Melt Distribution

Our compliance analysis improves constraints on crustal shear velocities within the EPR 9°–10°N segment. Compliance modeling suggests that a DLZ is present in the axial lower crust at 9°48′N and 9°33′N section of the EPR. The best fitting DLZ velocity is $Vs = 1.5$ km/s ($Vp = 4.5$ km/s) at 9°48′N and $Vs = 2.0$ km/s ($Vp = 5.2$ km/s) at 9°33′N. The DLZs are located at 4–7 km below the seafloor, beneath the bulk of the seismically imaged low-velocity zone [*Dunn et al*., 2000; *Vera et al*., 1990]. Our modeling suggests that the lateral extent of the DLZ is limited to within 4 km from the ridge axis.

The large velocity anomaly of the DLZ indicates the presence of elevated temperature and partial melt in the axial lower crust. Assuming a reference compressional velocity of 7.2 km/s for off-axis lower crust at 4–6 depth [*Dunn et al*., 2000; *Vera et al*., 1990], *Vp* of 4.5 km/s in the DLZ at 9°48′N corresponds to a 37% velocity reduction. In calculating the temperature effects on *Vp*, we use $\mathrm{d}\ln Vp/\mathrm{d}T = -14 \times 10^{-5} K^{-1}$, derived by *Dunn et al*. [2000] based on *Christensen* [1979] and *Karato* [1993] which takes into account anelastic effects. Assuming a reference off-axis temperature of 300°C at 4 km depth [*Henstock et al*., 1993] and a maximum temperature of 1195°C for the liquidus [*Sinton and Detrick*, 1992], only 34% of the total *Vp* anomaly (−0.89 km/s out of −2.7 km/s) in the 9°48′N DLZ (and 44% of the 9°33′N anomaly) can be explained by elevated temperatures alone.

The remaining velocity anomaly in the DLZ requires the presence of partial melt. Melt can exist in isolated pockets or in connected films and cracks. The geometry of the melt greatly affects the velocity reduction [*Faul et al*., 1994]. Melt in isolated spheres and ellipsoids produces much smaller velocity reduction than does melt in organized films at relaxed state [*Hammond and Humphreys*, 2000; *Schmeling*, 1985]. Different melt geometries also produce different relative fractional decreases of *Vs* and *Vp* ($\mathrm{d}\ln Vs/\mathrm{d}\ln Vp$). Melt in cracks and films generally yield a higher $\mathrm{d}\ln Vs/\mathrm{d}\ln Vp$ value than melt in textually equilibrated partially molten rocks [*Takei*, 2002]. Therefore, by combining *Vs* constraints from compliance with *Vp* constraints from prior seismic tomography studies, we can better constrain the amount and geometry of melt than can either method alone. In the axial lower crust (4–6 km) at 9°33′N, the *Vs* anomaly determined by compliance (48%–50%) and the *Vp* anomaly from seismic tomography (11%–25%) [*Dunn et al*., 2000] yield $\mathrm{d}\ln Vs/\mathrm{d}\ln Vp = 1.9 - 4.5$, which exceeds the predicted limit of $\mathrm{d}\ln Vs/\mathrm{d}\ln Vp = 1.5$ for textually equilibrated

partially molten rocks [*Takei*, 2002]. This indicates that melt in the DLZ may be predominantly stored in low aspect ratio films or cracks instead of isolated ellipsoidal pockets.

We use the results of *Hammond and Humphreys* [2000] to calculate the melt fraction in the DLZ from *Vs* anomalies. In the lower crust at 4 km depth, melt fraction in the DLZ at 9°48′N ranges from 11%–22% for isolated ellipsoids to 6–9% for film geometry. At 9°33′N, the inferred melt fractions are slightly lower: 7–14% for ellipsoids and 4–6% for films. This range of melt fractions (4%–14%) is roughly consistent with the estimates (5%–22%) from seismic tomography study at EPR 9°30′N [*Dunn et al*., 2000]. Near the base of the crust at 6 km depth, compliance modeling also suggests a large melt fraction: 7%–24% at 9°48′N and 5%–17% at 9°33′N. At this depth melt fraction estimated by compliance is larger than the estimate (2%–11%) by seismic tomography [*Dunn et al*., 2000].

Melts in the DLZ are likely stored in low aspect ratio bodies such as films, cracks, or sills. The elastic effects of connected sills and films should be equivalent if their dimensions are both smaller than the forcing wavelength [*Hudson*, 1981]. The depth of the DLZ approximately corresponds to the lower gabbroic section and the Moho transition zone at the Oman ophiolite [*Kelemen et al*., 1997]. Geochemical analysis of this section indicates that lower layered gabbros may be the remaining solid from which melt was extracted to form the upper crustal dikes and lavas [*Kelemen et al*., 1997; *Korenaga and Kelemen*, 1997]. It has been suggested that the lower crust at fast spreading ridges consists of multiple meter-scale magma sills, in which some portion of melt crystallizes in situ [*Kelemen et al*., 1997; *Korenaga and Kelemen*, 1997]. Several seismic reflection studies have imaged off-axis melt lenses near the Moho [*Canales et al*., 2009; *Nedimovic et al*., 2005] and in the midcrust [*Canales et al*., 2012]. Although we did not directly model the compliance of meter-scale molten sills, a previous 2-D modeling study by *Iassonov and Crawford* [2008] has shown that multiple low aspect ratio molten sills ($Vs \sim 0$) imbedded in a high-velocity lower crust can produce the same compliance anomaly as a region with constant low velocity. A series of thin, horizontal melt sills could also increase *Vp*/*Vs* ratio to up to 3.5 and produce strong transverse anisotropy [*Wang et al*., 2012], which can lead to significant *Vs* reduction but only moderate *Vp* reduction due to the different sensitivity of body wave refraction tomography and compliance [*Hulme et al*., 2003]. Therefore, the DLZ suggested by compliance modeling, along with the *Vp* imaged from seismic tomography, is consistent with the existence of aligned melt sills in the lower crust beneath 9°48′N and 9°33′N.

In addition to low aspect ratio melt geometry, anelastic effects may also contribute to the large ratio of *Vs* and *Vp* anomalies suggested by compliance and seismic tomography near 9°33′N, because the compliance observations are made at much lower frequency than active seismic wave tomography. The axial lower crust at EPR 9°–10°N has been shown to have strong attenuation [*Wilcock et al*., 1992]. The apparent velocity of attenuating partially molten rocks may be more strongly frequency dependent than that of melt-free rocks [*Aki and Richards*, 2002; *McCarthy et al*., 2011]. Therefore, the shear velocities at compliance frequencies (~0.01 Hz) may be lower than at the frequency of active seismic tomography (~5 Hz). We did not include this anelastic dispersion effect in building our shear velocity model, as an anelastic correction would require knowing the amplitude and frequency dependence of Q for rocks with partial melt, an area of much current uncertainty. The inferred melt fractions should be slightly smaller once this effect is properly accounted for.

5.2. Midcrustal LVZ

Compliance modeling suggests that in the axial midcrust (1.5–4 km deep), the LVZs at 9°48′N and 9°33′N are 5–7 km wide, consistent with active seismic tomography results [*Canales et al*., 2012; *Dunn et al*., 2000]. The minimum shear velocity in the LVZ is about 1.5 km/s immediately below the AML. Using a reference off-axis shear velocity of 3.5 km/s and temperature of 100°C at 1.5 km depth [*Henstock et al*., 1993], the velocity anomaly in the LVZ suggests a maximum melt fraction of 5% (film geometry) to 25% (ellipsoid geometry).

We used the *Vp* model from seismic tomography by *Dunn et al*. [2000] and the compliance data at 9°33′N to calibrate the *Vs*-*Vp* relationship in the LVZ. The calibration results suggest that $d\ln Vs/d\ln Vp$, the ratio between fraction changes in *Vs* and *Vp*, is close to 2.0 (a range of 1.8–2.2 gives good fit). This has important implications for the melt storage geometry in the LVZ, since $d\ln Vs/d\ln Vp = 2$ suggests that melt pockets likely have low aspect ratio (<0.01) [*Takei*, 2002]. The midcrustal LVZ is commonly considered a crystalline mush zone, in which melt are distributed along grain boundaries [*Wilcock et al*., 1992]. However, $d\ln Vs/d\ln Vp = 2$ exceeds the range for textually equilibrated partial melt (1–1.5) [*Takei*, 2002] and indicate that small cracks and sills may also exist in the LVZ. The existence of melt lenses within the LVZ has also been suggested by a recent active source seismic

study that revealed sub-AML reflectors [*Marjanovic et al*., 2013]. The calibration of the *Vs*-*Vp* relationship through the d ln *Vs*/d ln *Vp* ratio proves seafloor compliance to be a useful complimentary tool to seismic tomography in studying the physical properties of partially molten rocks. A small component of the large d ln *Vs*/d ln *Vp* value could be attributed to a larger anelastic effect on *Vs* than for *Vp* in regions with partial melt because of the lower frequencies used for compliance observations compared to frequencies used in the *P* wave tomography.

5.3. Along-Axis Variation of Crustal Melt Distribution and Implications for Melt Delivering Processes

Compliance modeling, combined with seismic reflection and tomography results [*Kent et al*., 1993a, 1993b; *Toomey et al*., 2007], allows a comprehensive assessment of the relationship between melt at different depths in the crust. A crustal LVZ corresponding to a partial melt zone is present along the ridge axis between 9°48′N and 9°08′N. The size, asymmetry, and amplitude of its velocity anomaly vary along the ridge, suggesting an along-axis variation of the melt distribution. The LVZs at 9°48′N and 9°33′N are of same width and melt fraction, with the lowest shear velocity of 1.5 km/s immediately below the AML. The LVZ at 9°48′N is centered beneath the ridge axis, while the LVZ at 9°33′N is centered about 0.6 km west of the ridge. Imaged widths of the AML at these two locations are relatively "normal" ($<$0.7 km at 9°48′N, 1–1.2 km near 9°33′N) [*Kent et al*., 1993a]. The LVZ shifts farther west to the south of the minor discontinuity at 9°18′N. At 9°18′N the LVZ is centered 2 km west of the ridge axis. The LVZ is highly asymmetric at 9°08′N, near the overlapping spreading center. The center of the LVZ is located approximately 1.5 km west of the ridge axis, but the low-velocity region is about twice as wide (13 km) as at 9°48′N, extending to 6–8 km west of the ridge axis. At both 9°18′N and 9°08′N an anomalously wide AML has been imaged (3.35–4.15 km) [*Kent et al*., 1993a, 1993b] extending from 0 to 4 km west of the ridge axis.

Although the LVZ is generally aligned with the AML along the ridge axis, the size and amount of melt in the LVZ inferred from compliance modeling do not show a systematic correlation with the width of the AML or its offset from the ridge axis. The LVZ at 9°18′N has the highest minimum shear velocity (*Vs* ~1.8 km/s) and probably contains the least amount of melt, whereas the LVZ at 9°08′N is twice as wide and probably contains the highest total volume of melt along EPR 9°–10°N. Both of these LVZs underlie a wide AML that extends approximately 4 km west of the ridge axis. Our observation is consistent with the proposed hypothesis that AML width is controlled by the transport pathway of melt to the axis rather than by the abundance of melt supply [*Kent et al*., 1993b].

A deep DLZ, possibly consisting of interconnected melt-filled sills or cracks, exists near the base of the lower crust at 9°33′N and 9°48′N, where the LVZ is centered close to rise axis and the AML is narrower. In contrast, near 9′08′N and 9°18′N where wider AMLs are imaged and LVZs are further offset from the ridge crest, less melt appears to accumulate in the lower crust, and no DLZ of size and melt anomaly similar to 9°48′N is detected (a small DLZ of width $<$ 2 km cannot be detected by compliance nor excluded). Although melts are negatively buoyant throughout the lower crust, they may be trapped in sills by permeability barriers [*Korenaga and Kelemen*, 1998]. The state of tectonic stress may control the existence of these permeability barriers. Near the OSC and spreading discontinuity where greater tectonic stress and higher crack density are expected, melt may penetrate through the crust more easily, and thus, the amount of melt retained in the lower crust is lower.

Crustal LVZs do not always align with the center of the uppermost mantle low-velocity zone (MLVZ) imaged from seismic tomography [*Toomey et al*., 2007], which shows along-axis variations rotated at a small angle from the ridge axis. However, the weakest LVZ at 9°18′N does correspond to the largest offset between the LVZ and the MLVZ, which is centered about 10 km east of the ridge axis (Figure 2b of *Toomey et al*. [2007]). The greater misalignment of mantle source and crustal accretion zone may lead to a less efficient melt transport and hence a reduced axial melt supply. On the other hand, the MLVZs at 9°48′N and 9°08′N are centered closer to ridge axis, producing a melt-rich LVZ. *Toomey et al*. [2007] concluded that the proximity of mantle melt supply to the ridge axis gives rise to enhanced on-axis magmatism and more hydrothermal venting. Our compliance results support this hypothesis by showing that LVZ has lower shear velocity thus more melt where ridge axis is centered above mantle melt source.

In summary, there appear to be two levels of control on melt distribution in the subaxial crust. The amount of melt entering the crustal accretion zone from the uppermost mantle source may be controlled by the proximity of the mantle melt source to the ridge axis [*Toomey et al*., 2007], where increasing offset between the morphological ridge axis and the focus of melt delivery in the mantle leads to decreasing melt fraction in

the crust. At the shallower level, the width of the AML, the offset of the LVZ from the axis, and the abundance of lower crustal melt (DLZ) may be governed by deformation due to the local tectonic stress state and its effect on permeability. Higher tectonic stress and higher permeability lead to efficient vertical melt transport and a wider AML, whereas lower stress may give rise to more melt retention in lower crustal sills.

5.4. Temporal Change of Melt Distribution in the Crust at 9°48′N: Implication for the Evolution of Magmatic System

Our compliance data provide direct geophysical evidence for short-term changes in melt distribution at a fast spreading ridge system. The on-axis compliances measured in 2007, after the 2005–2006 eruption, are significantly lower than values measured in 1999 (Figure 9a). Compliance modeling suggests that the decrease in compliance corresponds to up to 0.6 km/s increase in shear velocities (from 1.5 to 2.1 km/s) in the LVZ, (Figure 9b), suggesting a decreased amount of melt in the LVZ, implying that melt was extracted from the LVZ during this period (1999–2007). Using the same method [*Hammond and Humphreys*, 2000] to estimate the range of melt fractions, we infer that the maximum melt fraction in the LVZ decreases from 5–25% in 1999 to 2–9% in 2007. Even using the conservative assumption that melts are stored in thin films, this suggests up to 3% drop in melt fraction at the center of the LVZ (a relative decrease of 60%).

To quantify the change in total melt volume in the LVZ, we calculate the difference in melt fraction between the 1999 model and the 2007 model at each grid point and integrate the difference over the model to get the change in total melt volume. We assume a film geometry, which requires the least change of melt fraction (from 5% to 2%). We do not include possible changes in the DLZ melt fraction since the uncertainty of the DLZ velocities in the 2007 model is very high. Our calculation yields a melt volume decrease of $22 \times 10^5 m^3$ per meter of spreading ridge. If this decrease is constant along the 18 km of EPR ridge where new lava were documented [*Soule et al*., 2007], the total volume of melt decrease is estimated to be $3.93 \times 10^9 m^3$, 2 orders of magnitude larger than the estimated lava extracted from the AML during the 2005–2006 eruption ($4.7 \times 10^7 m^3$,[*Soule et al*., 2007]). Therefore it is highly possible that the decrease of melt fraction is localized near the measurement site at 9°48′N. On the other hand, a total volume of $4.7 \times 10^7 m^3$ of melt removed from the LVZ will only change the melt fraction by a maximum of 0.035% and the shear velocity by 0.007 km/s, which will have a negligible effect on compliance. Therefore, we conclude that the decrease of melt indicated by the change of compliance cannot be solely attributed to the extraction due to seafloor eruption. Several other mechanisms may contribute to the apparent decrease in melt fraction:

1. Melt Migration From LVZ to AML
   The dimensions of the AML and the heat output through hydrothermal activities require decadal melt replenishment of the AML to prevent it from completely freezing [*Ramondenc et al*., 2006]. Geochemical analysis of the erupted lava from the 2005–2006 eruption near EPR 9°48′N indicates that the 2005–2006 lavas represent residual melt from the 1991–1992 magmas mixed with melt within the crust, instead of newly injected, primitive mantle melt [*Goss et al*., 2010]. These studies indicate that AML may be replenished from sources within the crust. We suggest that melt migrating into the AML from the LVZ during the measurement gap period (1999–2007) may partially account for the decreased melt volume in the LVZ.

   Melt may migrate from the LVZ into the AML through two processes: fractional crystallization and posteruption replenishment. In the first process, magmas stored in the LVZ gradually migrate into the AML during the repose period leading up to the eruption (1992–2005) [*Goss et al*., 2010], resulting in a decrease of melt fraction in the LVZ. The migration of melt through the LVZ could be explained by a filter-pressing mechanism [*Natland and Dick*, 2001], in which settling crystals in the LVZ mush squeeze the fractionated liquids upward into the AML [*Mcbirney*, 1995]. However, on-axis compliance measurements in 1999 are nearly identical to measurements made in 1994 (Figure 9), while compliance measured in 2007 exhibit a significant decrease from 1999. It seems unlikely that the settling of crystals and upward flow of melt through this mechanism would greatly change rate after 1999 and before the eruption. It is possible, however, that the LVZ was replenished before 1999 by an episodic melt injection from mantle sources.

   A changing melt geometry may contribute to the apparent decrease of melt fraction. It was shown that as melt fraction decreases, the aspect ratio of melt pockets also change [*Faul et al*., 1994]. Therefore, if the melt geometry changes from film to spheroid as the melt fraction decreases, the apparent change of melt volume will be larger than the actual change.

In the second process, magma pressure drops in the AML during an eruption as magma is withdrawn to form the dikes and extrusive lava, creating a pressure gradient between the AML and the underlying melt reservoir in LVZ [*Nooner and Chadwick*, 2009]. In the months following an eruption, the magmas stored in the LVZ could be driven into the AML by this pressure gradient. From continuous monitoring of seafloor uplift at Axial Seamount on the Juan de Fuca Ridge, *Nooner and Chadwick* [2009] observed a rapid, exponential decaying seafloor uplift over the first year after the 1998 eruption. They proposed this mechanism to explain the rapid seafloor uplift. We suggest that the decrease of melt in the LVZ at the EPR may be partly caused by porous flow of melt into the AML driven by this posteruption pressure gradient. This process should occur on similar temporal scales as the rapid seafloor uplift recorded at Axial Seamount. Recharge of the LVZ would then occur more slowly during the following years. Repeated compliance measurements following an eruption in the future can help distinguish between these two processes.

We note that, however, the AML thickness would increase by ~360 m if all the melt removed from the LVZ was transferred to it (assuming a total cross-sectional melt volume of $2.2 \times 10^5 m^2$ and an AML width of 600 m [*Kent et al*., 1993a]). This is much thicker than any previous estimate of AML thickness at the EPR [*Collier and Singh*, 1998; *Kent et al*., 1990; *Xu et al*., 2014]. Therefore, melt migration into the AML can only account for part of the melt removed from the LVZ.

2. Feeding Off-Axis Magmatism From Axial LVZ
   It is possible that the melt in the LVZ also supplies off-axis magmatism at EPR. Previous studies have provided geophysical and geochemical evidences for off-axis volcanism at EPR 9°–10°N [*Goldstein et al*., 1994; *Troy Durant and Toomey*, 2009]. Recently, *Canales et al*. [2012] imaged a network of sills 4–8 km east of the ridge axis near 9°52′N. The off-axis sill network extends into the axial LVZ, indicating possible interaction between off-axis magmatic system and the axial melt sources. Although no current melt sills were imaged off axis 9°48′N, melt could migrate to off-axis regions as well as along-axis through preexisting fractures and pathways, leading to the decrease of melt fraction in the axial LVZ.
3. Decrease of Melt Fraction by Crystallization
   In addition to melt being removed from the LVZ into the AML or off-axis magmatic systems, melt can crystallize within the LVZ, leading to lower melt fraction and increasing velocities. The latent heat from the crystallization of melt is efficiently transported out of the magmatic system through vigorous hydrothermal circulation near and above the AML [*Morgan and Chen*, 1993; *Ramondenc et al*., 2006]. The rate of melt supply from the lower crustal and mantle sources may vary temporally, and melt injection may occur episodically rather than continuously. During period of abundant melt supply, the LVZ may contain a higher amount of melt, acting like a "buffer" between the AML and mantle source. During a period of reduced melt supply, the rate of crystallization could be faster than the rate of melt input, resulting in a decreasing amount of melt in the LVZ. The following scenario may be consistent with the compliance measurements and the seafloor observations: the EPR near 9°48′N underwent a period of high melt supply prior to 1999, leaving excess melt in the LVZ. After 1999, melt supply rate decreased, and more melt crystallized than was injected into the LVZ. Therefore, by 2007, the amount of melt in the LVZ had decreased. More time-dependent numerical modeling studies are needed to quantify the temporal variability of crustal melt fraction due to changing rate of supply and to validate this proposed mechanism.

As we discussed in section 4.4, unknown ocean wave directions may introduce some uncertainties to the estimated velocity change and melt fraction change between 1999 and 2007. Additional uncertainty in the change of melt fraction comes from the uncertainty (maximum 10%) in the gain for the pressure data used for the 1994/1999 compliance data. Lower gain values would imply lower compliance values in 1994 and 1999 leading to lower melt fraction estimate in the LVZ before the eruption, reducing the inferred change in melt volume. Even with this uncertainty, the flattening of the compliance curve (Figure 9) between 1999 and 2007 requires an increase of shear velocities in the LVZ.

5.5. Implications for EPR Crustal Accretion

Our compliance data and modeling provide new constraints on the melt distribution and crustal accretion mechanism at fast spreading ridges. Of the existing two end-member models, the gabbro glacier model suggests that the entire oceanic crust section was formed by the crystallization and subsidence of melt at the shallow AML [*Morgan and Chen*, 1993; *Quick and Denlinger*, 1993], while the multisills model suggests that a substantial portion of the lower layered gabbros may have formed through crystallization of melt in sills within the lower crust [*Boudier et al*., 1997; *Kelemen et al*., 1997; *Korenaga and Kelemen*, 1998]. Compliance

modeling indicates that regions of low shear velocity (DLZ) and high melt fraction exist in the lower crust (4–7 km) beneath at least part of the EPR between 9° and 10°N. Melts in the DLZ are likely stored in low aspect ratio films or sills. A portion of melt in the DLZ may crystallize in the sills and subsequently move horizontally away from the ridge, while the remaining melt is transported to either shallower sills or the AML. As the melt moves upward, new permeability barriers may form on a slope at the crystallization front, guiding the melt toward a narrower region [*Hebert and Montesi*, 2011]. As melt volume fraction (porosity) increases, sills may become smaller and interconnected and transition into a more isotropic crystalline mush. Melt in the mush zone is then driven upward by negative buoyancy through porous flow, until encountering the hydrothermal cooling front and accumulating in a shallow AML.

The midcrustal LVZ beneath the AML is probably the largest melt reservoir in the axial crust. A LVZ is present at all cross sections of compliance measurement sites, but the size and amount of melt in the LVZ vary from place to place. Recent geochemical analysis of melt inclusion samples at the EPR and the Juan de Fuca Ridge indicates that the majority of phenocrysts in erupted lavas crystallized at depths corresponding to the AML and the LVZ [*Wanless and Shaw*, 2012], but this does not preclude significant crystallization at greater depth, since melts crystallized in deeper crust are less likely to be entrained into the AML and erupted. Given the observed variability of the existence of DLZ and the AML width, we suggest that the portion of lower crust formed in situ at the EPR may vary from place to place. Both the gabbros glacier model and the multisill model could be valid in explaining the formation of the lower crust at fast-to-intermediate spreading centers. The relative importance of the two mechanisms may depend on the local crustal stress state and deviation of mantle melt supply from the ridge axis.

6. Conclusion

We have analyzed seafloor compliance measured at 61 sites over four expeditions and a 15 year time span, using three-dimensional seafloor compliance modeling to estimate the shear velocity structure of the crust and uppermost mantle at EPR 9°–10°N.

Compliance measurements at 9°48′N and 9°33′N suggest a deep low-velocity zone (DLZ) in the lower crust, consistent with a region of high melt fraction. Considering the ratio of *Vs* anomaly from compliance and *Vp* anomaly from seismic tomography, we suggest that the melt in the lower crust may be stored in connected films or sills rather than in isolated pockets.

Repeated compliance measurements at 9°48′N provide direct evidence that the magmatic tapping system at the EPR evolves over a less than decadal time scale. The observed temporal changes of compliance at 9°48′N between prior to and after the 2005–2006 eruption indicate a significant decrease of the melt fraction in the midcrustal LVZ. The inferred decrease of melt volume significantly exceeds the estimated volume of erupted lava and dike from the eruption. Mechanisms that can explain the decrease of melt fraction include melt migration from LVZ to AML, the feeding of off-axis magmatic systems, and crystallization within the LVZ. More repeated compliance measurements in this area or a continuous monitoring system throughout an eruption cycle are needed to distinguish between these mechanisms and to further understand the evolution of the magmatic system in intermediate to fast spreading ridges.

Compliance measurements at four cross-axis lines along the EPR 9°–10°N reveal significant variation of crustal melt distribution along the ridge. Sizes and shear velocities of crustal LVZ inferred from compliance do not exhibit a strong correlation with the width of the imaged AML. DLZs seem to exist where AMLs are narrower and mantle melt zones are centered beneath the ridge. These variations suggest that the amount of lower crustal melt is likely governed by the crustal stress and permeability, rather than the abundance of mantle melt supply. Both the gabbro glacier model and the multisill model could be valid in explaining the formation of the lower crust at fast-to-intermediate spreading centers. The relative importance of the two relies on the crustal stress state and deviation of mantle melt supply from the ridge axis.

Acknowledgments
The compliance data were collected during several cruises on the R/V *Atlantis*, and we thank the captain and crew for their tireless help. The compliance data can be obtained by contacting the corresponding author. The finite element code *Pylith* used in this work is obtained free of charge from the Computational Infrastructure for Geodynamics. We thank Robert Dunn and Peter Kelemen for their insightful comments. J. Pablo Canales and an anonymous reviewer provided careful reviews that significantly improved this manuscript. This research was supported by the National Science Foundation grant OCE04-26372.

References

Aagaard, B., C. Williams, and M. Knepley (2008), PyLith: A finite-element code for modeling quasi-static and dynamic crustal deformation, *Eos Trans. AGU*, *1*, 1925, Fall Meet. Suppl., Abstract #T41A-1925.

Aki, K., and P. G. Richards (2002), *Quantitative Seismology*, 2nd ed., xviii, 700 pp., Univ. Science Books, Sausalito, Calif.

Barth, G. A., and J. C. Mutter (1996), Variability in oceanic crustal thickness and structure: Multichannel seismic reflection results from the northern East Pacific Rise, *J. Geophys. Res.*, *101*(B8), 17,951–17,975, doi:10.1029/96JB00814.

Bazin, S., A. Harding, G. Kent, J. Orcutt, S. Singh, C. Tong, J. Pye, P. Barton, M. Sinha, and R. White (2003), A three-dimensional study of a crustal low velocity region beneath the 9°03′N overlapping spreading center, *Geophys. Res. Lett.*, *30*(2), 1039, doi:10.1029/2002GL015137.

Boudier, F., A. Nicolas, B. Ildefonse, and D. Jousselin (1997), EPR microplates, a model for the Oman ophiolite, *Terra Nova*, *9*(2), 79–82.
Bowles, J., J. S. Gee, D. V. Kent, M. R. Perfit, S. A. Soule, and D. J. Fornari (2006), Paleointensity applications to timing and extent of eruptive activity, 9°–10°N East Pacific Rise, *Geochem. Geophys. Geosyst.*, *7*, Q06006, doi:10.1029/2005GC001141.
Canales, J. P., R. S. Detrick, D. R. Toomey, and W. S. D. Wilcock (2003), Segment-scale variations in the crustal structure of 150–300 kyr old fast spreading oceanic crust (East Pacific Rise, 8 degrees 15'N–10 degrees 5'N) from wide-angle seismic refraction profiles, *Geophys. J. Int.*, *152*(3), 766–794.
Canales, J. P., M. R. Nedimovic, G. M. Kent, S. M. Carbotte, and R. S. Detrick (2009), Seismic reflection images of a near-axis melt sill within the lower crust at the Juan de Fuca ridge, *Nature*, *460*(7251), 89–93, doi:10.1038/nature08095.
Canales, J. P., H. Carton, S. M. Carbotte, J. C. Mutter, M. R. Nedimovic, M. Xu, O. Aghaei, M. Marjanovic, and K. Newman (2012), Network of off-axis melt bodies at the East Pacific Rise, *Nat. Geosci.*, *5*(4), 279–283, doi:10.1038/ngeo1377.
Carbotte, S. M., M. Marjanovic, H. Carton, J. C. Mutter, J. P. Canales, M. R. Nedimovic, S. S. Han, and M. R. Perfit (2013), Fine-scale segmentation of the crustal magma reservoir beneath the East Pacific Rise, *Nat. Geosci.*, *6*(10), 866–870, doi:10.1038/Ngeo1933.
Chadwick, W. W., S. L. Nooner, M. A. Zumberge, R. W. Embley, and C. G. Fox (2006), Vertical deformation monitoring at Axial Seamount since its 1998 eruption using deep-sea pressure sensors, *J. Volcanol. Geotherm. Res.*, *150*(1–3), 313–327, doi:10.1016/j.jvolgeores.2005.07.006.
Chadwick, W. W., S. L. Nooner, D. A. Butterfield, and M. D. Lilley (2012), Seafloor deformation and forecasts of the April 2011 eruption at Axial Seamount, *Nat. Geosci.*, *5*(7), 474–477, doi:10.1038/ngeo1464.
Christensen, N. I. (1979), Compressional wave velocities in rocks at high-temperatures and pressures, critical thermal-gradients, and crustal low-velocity zones, *J. Geophys. Res.*, *84*(B12), 6849–6857, doi:10.1029/Jb084ib12p06849.
Christensen, N. I., and G. H. Shaw (1970), Elasticity of mafic rocks from the Mid-Atlantic Ridge, *Geophys. J. R. Astron. Soc.*, *20*(3), 271–284.
Collier, J. S., and S. C. Singh (1998), A seismic inversion study of the axial magma chamber reflector beneath the East Pacific Rise near 10 N, *Geol. Soc. London Spec. Publ.*, *148*(1), 17–28.
Crawford, W. C., and S. C. Webb (2002), Variations in the distribution of magma in the lower crust and at the Moho beneath the East Pacific Rise at 9–10 N, *Earth Planet. Sci. Lett.*, *203*(1), 117–130, doi:10.1016/S0012-821X(02)00831-2.
Crawford, W. C., S. C. Webb, and J. A. Hildebrand (1991), Seafloor compliance observed by long-period pressure and displacement measurements, *J. Geophys. Res.*, *96*(B10), 16,151–16,160, doi:10.1029/91JB01577.
Crawford, W. C., S. C. Webb, and J. A. Hildebrand (1998), Estimating shear velocities in the oceanic crust from compliance measurements by two-dimensional finite difference modeling, *J. Geophys. Res.*, *103*(B5), 9895–9916, doi:10.1029/97JB03532.
Crawford, W. C., S. C. Webb, and J. A. Hildebrand (1999), Constraints on melt in the lower crust and Moho at the East Pacific Rise, 9°48'N, using seafloor compliance measurements, *J. Geophys. Res.*, *104*(B2), 2923–2939, doi:10.1029/1998JB900087.
Crawford, W. C., S. C. Singh, T. Hulme, and J. R. Smallwood (2005), Applications of seafloor compliance measurements in the Faroes-Shetland Basin, *Faroe Isl. Explor. Conf.*, *43*, 32–43.
Detrick, R. S., P. Buhl, E. Vera, J. Mutter, J. Orcutt, J. Madsen, and T. Brocher (1987), Multichannel seismic imaging of a crustal magma chamber along the East Pacific Rise, *Nature*, *326*(6108), 35–41.
Dunn, R. A., D. R. Toomey, and S. C. Solomon (2000), Three-dimensional seismic structure and physical properties of the crust and shallow mantle beneath the East Pacific Rise at 9°30'N, *J. Geophys. Res.*, *105*(B10), 23,537–23,555, doi:10.1029/2000JB900210.
Faul, U. H., D. R. Toomey, and H. S. Waff (1994), Intergranular basaltic melt is distributed in thin, elongated inclusions, *Geophys. Res. Lett.*, *21*(1), 29–32.
Fornari, D. J., R. M. Haymon, M. R. Perfit, T. K. P. Gregg, and M. H. Edwards (1998), Axial summit trough of the east Pacific rise 9 degrees–10 degrees N: Geological characteristics and evolution of the axial zone on fast spreading mid-ocean ridges, *J. Geophys. Res.*, *103*(B5), 9827–9855.
Garmany, J. (1989), Accumulations of melt at the base of young oceanic crust, *Nature*, *340*(6235), 628–632.
Goldstein, S. J., M. R. Perfit, R. Batiza, D. J. Fornari, and M. T. Murrell (1994), Off-axis volcanism at the East Pacific Rise detected by uranium-series dating of basalts, *Nature*, *367*(6459), 157–159.
Goss, A. R., M. R. Perfit, W. I. Ridley, K. H. Rubin, G. D. Kamenov, S. A. Soule, A. Fundis, and D. J. Fornari (2010), Geochemistry of lavas from the 2005–2006 eruption at the East Pacific Rise, 9°46'N–9°56'N: Implications for ridge crest plumbing and decadal changes in magma chamber compositions, *Geochem. Geophys. Geosyst.*, *11*, Q05T09, doi:10.1029/2009GC002977.
Hammond, W. C., and E. D. Humphreys (2000), Upper mantle seismic wave velocity: Effects of realistic partial melt geometries, *J. Geophys. Res.*, *105*(B5), 10,975–10,986, doi:10.1029/2000JB900041.
Han, S., S. M. Carbotte, H. Carton, J. C. Mutter, O. Aghaei, M. R. Nedimović, and J. P. Canales (2014), Architecture of on- and off-axis magma bodies at EPR 9°37–40'N and implications for oceanic crustal accretion, *Earth Planet. Sci. Lett.*, *390*, 31–44, doi:10.1016/j.epsl.2013.12.040.
Harding, A. J., G. M. Kent, and J. A. Orcutt (1993), A multichannel seismic investigation of upper crustal structure at 9°N on the East Pacific Rise—Implications for crustal accretion, *J. Geophys. Res.*, *98*(B8), 13,925–13,944, doi:10.1029/93JB00886.
Haymon, R. M., et al. (1993), Volcanic eruption of the mid-ocean ridge along the East Pacific Rise crest at 9-Degrees–45–52'N—Direct submersible observations of seafloor phenomena associated with an eruption event in April, 1991, *Earth Planet. Sci. Lett.*, *119*(1–2), 85–101, doi:10.1016/0012-821x(93)90008-W.
Hebert, L. B., and L. G. J. Montesi (2011), Melt extraction pathways at segmented oceanic ridges: Application to the East Pacific Rise at the Siqueiros transform, *Geophys. Res. Lett.*, *38*, L11306, doi:10.1029/2011GL047206.
Henstock, T. J., A. W. Woods, and R. S. White (1993), The accretion of oceanic crust by episodic sill intrusion, *J. Geophys. Res.*, *98*(B3), 4143–4161.
Hudson, J. A. (1981), Wave speeds and attenuation of elastic waves in material containing cracks, *Geophys. J. R. Astron. Soc.*, *64*(1), 133–150.
Hulme, T., A. E. Ricolleau, S. Bazin, W. C. Crawford, and S. C. Singh (2003), Shear wave structure from joint analysis of seismic and seafloor compliance data, *Geophys. J. Int.*, *155*(2), 514–520, doi:10.1046/J.1365-246x.2003.02061.X.
Hulme, T., W. C. Crawford, and S. C. Singh (2005), The sensitivity of seafloor compliance to two-dimensional low-velocity anomalies, *Geophys. J. Int.*, *163*(2), 547–558, doi:10.1111/j.1365-246X.2005.02753.x.
Iassonov, P., and W. Crawford (2008), Two-dimensional finite-difference model of seafloor compliance, *Geophys. J. Int.*, *174*(2), 525–541, doi:10.1111/j.1365-246X.2008.03782.x.
Kampfmann, W., and H. Berckhemer (1985), High temperature experiments on the elastic and anelastic behaviour of magmatic rocks, *Phys. Earth Planet. Inter.*, *40*, 223–470.
Karato, S. (1993), Importance of anelasticity in the interpretation of seismic tomography, *Geophys. Res. Lett.*, *20*(15), 1623–1626, doi:10.1029/93GL01767.
Kelemen, P. B., K. Koga, and N. Shimizu (1997), Geochemistry of gabbro sills in the crust-mantle transition zone of the Oman ophiolite: Implications for the origin of the oceanic lower crust, *Earth Planet. Sci. Lett.*, *146*(3–4), 475–488.
Kent, G. M., A. J. Harding, and J. A. Orcutt (1990), Evidence for a smaller magma chamber beneath the East Pacific Rise at 9-Degrees-30'N, *Nature*, *344*(6267), 650–653, doi:10.1038/344650a0.
Kent, G. M., A. J. Harding, and J. A. Orcutt (1993a), Distribution of magma beneath the East Pacific Rise between the Clipperton Transform and the 9°17'N Deval from forward modeling of common depth point data, *J. Geophys. Res.*, *98*(B8), 13,945–13,969.

Kent, G. M., A. J. Harding, and J. A. Orcutt (1993b), Distribution of magma beneath the East Pacific Rise near the 9°03′N overlapping spreading center from forward modeling of common depth point data, *J. Geophys. Res.*, *98*(B8), 13,971–13,995.
Kent, G. M., et al. (2000), Evidence from three-dimensional seismic reflectivity images for enhanced melt supply beneath mid-ocean-ridge discontinuities, *Nature*, *406*(6796), 614–618.
Korenaga, J., and P. B. Kelemen (1997), Origin of gabbro sills in the Moho transition zone of the Oman ophiolite: Implications for magma transport in the oceanic lower crust, *J. Geophys. Res.*, *102*(B12), 27,729–27,749.
Korenaga, J., and P. B. Kelemen (1998), Melt migration through the oceanic lower crust: A constraint from melt percolation modeling with finite solid diffusion, *Earth Planet. Sci. Lett.*, *156*(1–2), 1–11.
Macdonald, K. C., P. J. Fox, L. J. Perram, M. F. Eisen, R. M. Haymon, S. P. Miller, S. M. Carbotte, M. H. Cormier, and A. N. Shor (1988), A new view of the mid-ocean ridge from the behavior of ridge-axis discontinuities, *Nature*, *335*(6187), 217–225, doi:10.1038/335217a0.
Marjanovic, M., S. M. Carbotte, H. Carton, J. C. Mutter, M. R. Nedimovic, and J. P. Canales (2013), Seismic images of multiple magma sills beneath the East Pacific Rise, *Eos Trans. AGU*, Fall Meet. Suppl., Abstract #OS42A-05.
Mcbirney, A. R. (1995), Mechanisms of differentiation in the Skaergaard Intrusion, *J. Geol. Soc. London*, *152*, 421–435.
McCarthy, C., and Y. Takei (2011), Anelasticity and viscosity of partially molten rock analogue: Toward seismic detection of small quantities of melt, *Geophys. Res. Lett.*, *38*, L18306, doi:10.1029/2011GL048776.
McCarthy, C., Y. Takei, and T. Hiraga (2011), Experimental study of attenuation and dispersion over a broad frequency range: 2. The universal scaling of polycrystalline materials, *J. Geophys. Res.*, *116*, B09207, doi:10.1029/2011JB008384.
Moores, E. M., and F. J. Vine (1971), Troodos Massif, Cyprus, and other ophiolites as oceanic crust—Evaluation and implications, *Philos. Trans. R. Soc A*, *268*(1192), 443–467.
Morgan, J. P., and Y. J. Chen (1993), The genesis of oceanic crust: Magma injection, hydrothermal circulation, and crustal flow, *J. Geophys. Res.*, *98*(B4), 6283–6297, doi:10.1029/92JB02650.
Mutter, J. C., G. A. Barth, P. Buhl, R. S. Detrick, J. Orcutt, and A. Harding (1988), Magma distribution across ridge-axis discontinuities on the East Pacific Rise from multichannel seismic images, *Nature*, *336*(6195), 156–158, doi:10.1038/336156a0.
Natland, J. H., and H. J. B. Dick (2001), Formation of the lower ocean crust and the crystallization of gabbroic cumulates at a very slowly spreading ridge, *J. Volcanol. Geotherm. Res.*, *110*(3–4), 191–233, doi:10.1016/S0377-0273(01)00211-6.
Nedimovic, M. R., S. M. Carbotte, A. J. Harding, R. S. Detrick, J. P. Canales, J. B. Diebold, G. M. Kent, M. Tischer, and J. M. Babcock (2005), Frozen magma lenses below the oceanic crust, *Nature*, *436*(7054), 1149–1152, doi:10.1038/nature03944.
Nooner, S. L., and W. W. Chadwick (2009), Volcanic inflation measured in the caldera of Axial Seamount: Implications for magma supply and future eruptions, *Geochem. Geophys. Geosyst.*, *10*, Q02002, doi:10.1029/2008GC002315.
Perfit, M. R., and W. Chadwick (1998), Magmatism at mid-ocean ridges: Constraints from volcanological and geochemical investigations, *Geophys. Monogr. AGU*, *106*, 59–116.
Quick, J. E., and R. P. Denlinger (1993), Ductile deformation and the origin of layered gabbro in ophiolites, *J. Geophys. Res.*, *98*(B8), 14,015–14,027, doi:10.1029/93JB00698.
Ramondenc, P., N. G. A. Leonid, K. L. Von Damm, and R. P. Lowell (2006), The first measurements of hydrothermal heat output at 9°50′N, East Pacific Rise, *Earth Planet. Sci. Lett.*, *245*(3–4), 487–497, doi:10.1016/J.Epsl.2006.03.023.
Schmeling, H. (1985), Numerical models on the influence of partial melt on elastic, anelastic and electric properties of rocks. 1. Elasticity and anelasticity, *Phys. Earth Planet. Inter.*, *41*(1), 34–57.
Singh, S. C., G. M. Kent, J. S. Collier, A. J. Harding, and J. A. Orcutt (1998), Melt to mush variations in crustal magma properties along the ridge crest at the southern East Pacific Rise, *Nature*, *394*(6696), 874–878.
Sinton, J. M., and R. S. Detrick (1992), Mid-ocean ridge magma chambers, *J. Geophys. Res.*, *97*(B1), 197–216.
Sinton, J. M., E. Bergmanis, K. Rubin, R. Batiza, T. K. P. Gregg, K. Gronvold, K. C. Macdonald, and S. M. White (2002), Volcanic eruptions on mid-ocean ridges: New evidence from the superfast spreading East Pacific Rise, 17°–19°S, *J. Geophys. Res.*, *107*(B6), 2115, doi:10.1029/2000JB000090.
Soule, S. A., D. J. Fornari, M. R. Perfit, and K. H. Rubin (2007), New insights into mid-ocean ridge volcanic processes from the 2005–2006 eruption of the East Pacific Rise, 9°46′N–9°56′N, *Geology*, *35*(12), 1079, doi:10.1130/g23924a.1.
Takei, Y. (2002), Effect of pore geometry on V-P/V-S: From equilibrium geometry to crack, *J. Geophys. Res.*, *107*(B2), 2043, doi:10.1029/2001JB000522.
Tolstoy, M., A. J. Harding, J. A. Orcutt, R. S. Detrick, G. M. Kent, J. C. Mutter, and P. Buhl (1997), Deepening of the axial magma chamber on the southern East Pacific Rise toward the Garrett Fracture Zone, *J. Geophys. Res.*, *102*(B2), 3097–3108.
Tolstoy, M., et al. (2006), A seafloor spreading event captured by seismometers, *Science*, *314*(5807), 1920–1922, doi:10.1126/Science.1133950.
Tong, C. H., et al. (2003), Influence of enhanced melt supply on upper crustal structure at a mid-ocean ridge discontinuity: A three-dimensional seismic tomographic study of 9°N East Pacific Rise, *J. Geophys. Res.*, *108*(B10), 2464, doi:10.1029/2002JB002163.
Toomey, D. R., S. C. Solomon, and G. M. Purdy (1994), Tomographic imaging of the shallow crustal structure of the East Pacific Rise at 9°30′N, *J. Geophys. Res.*, *99*(B12), 24,135–24,157.
Toomey, D. R., D. Jousselin, R. A. Dunn, W. S. D. Wilcock, and R. Detrick (2007), Skew of mantle upwelling beneath the East Pacific Rise governs segmentation, *Nature*, *446*(7134), 409–414, doi:10.1038/nature05679.
Troy Durant, D., and D. R. Toomey (2009), Evidence and implications of crustal magmatism on the flanks of the East Pacific Rise, *Earth Planet. Sci. Lett.*, *287*(1–2), 130–136, doi:10.1016/j.epsl.2009.08.003.
Vera, E. E., J. C. Mutter, P. Buhl, J. A. Orcutt, A. J. Harding, M. E. Kappus, R. S. Detrick, and T. M. Brocher (1990), The structure of 0-My to 0.2-My old oceanic crust at 9°N on the East Pacific Rise from expanded spread profiles, *J. Geophys. Res.*, *95*(B10), 15,529–15,556.
Wang, X. Q., A. Schubnel, J. Fortin, E. C. David, Y. Gueguen, and H. K. Ge (2012), High Vp/Vs ratio: Saturated cracks or anisotropy effects?, *Geophys. Res. Lett.*, *39*, L11307, doi:10.1029/2012GL051742.
Wanless, V. D., and A. M. Shaw (2012), Lower crustal crystallization and melt evolution at mid-ocean ridges, *Nat. Geosci.*, *5*(9), 651–655, doi:10.1038/Ngeo1552.
Webb, S. C., X. Zhang, and W. Crawford (1991), Infragravity waves in the deep ocean, *J. Geophys. Res.*, *96*(C2), 2723–2736.
Wilcock, W. S. D., S. C. Solomon, G. M. Purdy, and D. R. Toomey (1992), The seismic attenuation structure of a fast-spreading mid-ocean ridge, *Science*, *258*(5087), 1470–1474.
Williams, C. A. (2006), Development of a package for modeling stress in the lithosphere, *Eos Trans. AGU*, *87*(36), Jt. Assem. Suppl., Abstract T24A-01.
Williams, C. A., B. Aagaard, and M. G. Knepley (2005), Development of software for studying earthquakes across multiple spatial and temporal scales by coupling quasi-static and dynamic simulations, *Eos Trans. AGU*, *89*(53), Fall Meet. Suppl., Abstract S53A-1072.
Xu, M., J. P. Canales, S. M. Carbotte, H. Carton, M. R. Nedimović, and J. C. Mutter (2014), Variations in axial magma lens properties along the East Pacific Rise (9°30′–10°00′N) from swath 3-D seismic imaging and 1-D waveform inversion, *J. Geophys. Res. Solid Earth*, doi:10.1002/2013JB010730.